Development of a Predictive Model for the Design of Parts Fabricated by Fused Deposition Modeling

---

A Thesis presented to the Faculty of the Graduate School at the University of Missouri-Columbia

---

In Partial Fulfillment of the Requirements for the Degree

Master of Science

---

by

BRIAN GRAYBILL

Dr. A. Sherif El-Gizawy, Thesis Supervisor

MAY 2010

The undersigned, appointed by the dean of the Graduate School, have examined the thesis entitled

DEVELOPMENT OF A PREDICTIVE MODEL FOR THE DESIGN OF PARTS FABRICATED BY FUSED DEPOSITION MODELING

presented by Brian Graybill

a candidate for the degree Master of Science,

and hereby certify that, in their opinion, it is worthy of acceptance.

_____

Professor Hani Salim

_____

Professor Jinn-Kuen Chen

_____

Professor A. Sherif El-Gizawy

Thanks to my Lord Jesus, who gives me life everyday by his grace, and without whom I would be nothing. Thanks also to my parents, who love and support me ceaselessly and unconditionally. I am blessed to be your son.

ACKNOWLEDGEMENTS

First, I would like to thank the Boeing Company for their sponsorship of this research. In addition to funding the work, Boeing also providing the use of their own fused deposition modeling machines and raw material. Without their willingness to participate, this project could not have been completed.

I would also like to acknowledge the technical experts who were invaluable to this project. Michael Hayes, Gregg Bogucki, and Dave Dietrich from the Boeing Company all provided technical expertise and guidance throughout the project. They were all readily available when questions arose and always willing to help. A special thanks to Mark Sanner from Sabic Innovative plastics as well for his immediate and overwhelming response to questions regarding Ultem 9085.

Thank you as well to all those at the University of Missouri-Columbia who aided this project. First, thank you to my advisor, Dr. A. Sherif El-Gizawy. His flexibility has allowed me to pursue my interests outside of academia while still helping me maintain progress towards my degree. His guidance and encouragement have led me to accomplish work that I am proud of and that is beneficial to the engineering field. My research partners, Joseph Cardona and Clayton Zak, have also proved to be invaluable resources because of their ideas and hard work. Finally, an enormous debt of gratitude is extended to Rex Gish and Richard Oberto, who work ceaselessly and tirelessly to ensure that the students at the University of Missouri-Columbia have the tools they need to complete their research.

Table of Contents

LIST OF ILLUSTRATIONS

Figure **Page**

Table **Page**

ABSTRACT

Fused deposition modeling, or FDM, is a direct digital manufacturing process that is used to rapidly fabricate prototype parts with thermoplastic materials. While rapid manufacturing processes like FDM are currently being used to produce prototypes, various industries are interested in developing these technologies to a degree that would allow for end-use parts to be created. Fused deposition modeling is of particular interest in the maturing of rapid prototyping to rapid manufacturing due to its simple fabrication method and variety of usable materials such as polyphenylsulfone (PPSF) and Ultem 9085, which are both of interest because their desirable strength characteristics.

In order to fully develop FDM from rapid prototyping to rapid manufacturing, a model must exist to predict final part behavior. This work accomplishes the first critical step in such a model by employing a combined heat transfer and sintering model to predict the bond length between adjacent filaments. By comparing the predicted values to actual bond lengths (observed from microscope images), the model is found to be moderately accurate, but limited. The discrepancy between predicted and observed values is attributed to creep.

Another limitation currently experienced by FDM parts is the reduced strength in the out of plane axis (z-axis). To characterize the process parameters that affect z-axis strength, a Taguchi experimental matrix was applied to PPSF tensile specimens consisting of single bonds in the z-direction. Analysis showed extrusion temperature to be statistically significant. In an effort to improve bond length and the strength of the bonds, an annealing procedure was applied to z-axis tensile specimens fabricated from Ultem 9085. Though the post-processing treatment increased bond length, bond strength is actually decreased due to thermal degradation.

The current work therefore offers another step in the development of FDM through the modeling of the process and the testing and post-processing of its resultant parts. The results not only give direction for future refinements in modeling, but also reveal the importance of extrusion temperature in regard to the z-axis strength. Annealing is found to have detrimental effects resulting from thermal degradation, which is another aspect of FDM that deserves attention in the course of its development. Thus, the current work does not complete the prediction of FDM part behavior, but provides a reference for future researchers seeking to participate in transition of FDM from rapid prototyping to rapid manufacturing technology.

1. Introduction

Rapid prototyping (RP) is a term used to describe a relatively new class of manufacturing processes. These processes fabricate a part by adding material in thin cross-sections until the part is built (which is why these processes are also referred to as layered manufacturing (LM)). Rapid prototyping is advantageous in many ways. One of the benefits most often cited is the ability to create part geometries that are impossible with conventional methods (e.g. ducting with internal features). These parts can also be built almost directly from a computer-aided design (CAD) and completed within hours. This, in combination with the fact that no expensive tools are required to produce a part dramatically reduces lead times that would otherwise be required to produce a prototype. Additionally, RP processes use much less material than conventional methods because fabrication is a result of adding material instead of removing it, thus reducing waste.

The benefits of RP processes make them an attractive option not only for prototype parts, but also for end-use parts. There are several industries with a very high interest in developing RP technology into rapid manufacturing (RM) technology, such that an RP process can be used to create parts to be put into service. Examples of these industries are the biomedical field, which could employ RM to create bone splints specific to an individual in a matter of hours, and the aerospace industry, which typically manufactures in low volumes and would have use for parts with complex geometries. However, while there is significant desire to use LM for

manufacturing, the technologies currently being used must be further developed and understood in order to design safe, robust parts that are fabricated with RM processes.

One RP process with considerable potential is fused deposition modeling (FDM, see Fig. 1.1). This process creates parts by extruding an amorphous polymeric filament through a heated nozzle and depositing semi-molten filament on a work table. Several filaments are deposited in succession to create a single layer; then, the work table moves in the negative z direction to allow for deposition of the next layer. The simplicity of this fabrication process, along with the wide variety of materials available to FDM users, are a few of the reasons for FDM's popularity.

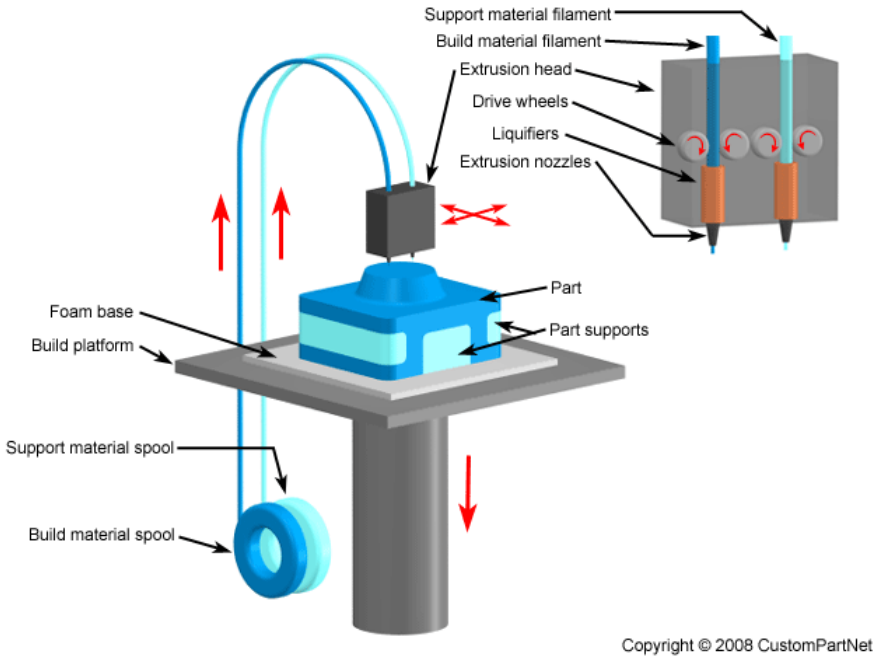

Fig. 1.1. Graphical representation of the FDM process [1].

Much work has already been done in the area of characterizing and optimizing the FDM process. Kulkarni and Dutta investigated the effect of extrusion pattern on part stiffness [2]. Pennington,

Hoekstra, and Newcomer found that part size, location in the work envelope, and oven temperature during the build all had significant effects on dimensional accuracy [3]. Reddy, Reddy, and Ghosh determined that road gap, extrusion temperature, and oven temperature all had a significant impact on part strength for parts fabricated from acrylo-nitrile butadiene styrene (ABS), a finding that holds for most materials [4]. Sun et al. researched the effect of processing conditions on bonding quality (which is critical to part strength) [5]. Warp deformation in FDM parts was characterized by Wang, Xi, and Jin and attributed to thermal stresses caused during deposition [6]. However, while this work is useful in determining how to create stronger parts, a model capable of predicting FDM part behavior is still lacking.

It is well known that the strength of bonds between filaments is largely connected to the neck size between the filaments. In turn, the neck size is almost entirely dependent on the thermal history of the filament, as temperature is the driving force behind the molecular diffusion that causes the neck to form. In an attempt to model the heat transfer taking place during deposition, Yardimci et al developed 1- and 2-dimensional analytical models for a single filament [7]. This model has been used in many other works, including those which coupled the thermal predictions of a filament with a modified Frenkel model [8], such as the analysis completed by Pokluda et al. [9]. Predictive modeling has also been investigated on a macro-level. The filament mesostructure of FDM parts is analogous to the fiber layout in composite materials. As such, various researchers have attempted to apply classical lamination theory to predict the failure criteria of FDM parts [10, 11]. Moderate accuracy was achieved with these equations. Three-dimensional finite element analysis (FEA) is another method being explored in the prediction of the mechanical behavior of FDM parts. Finite element software can also help with the thermal analysis of the FDM process. In fact, some packages, such as ANSYS, can model the whole process by coupling the thermal and mechanical physics, as shown by Zhang and Chou

[13, 14], who modeled process induced stress (caused by rapid heating and cooling) with this method.

Following the idea that FDM parts resemble composite materials, research has also been conducted in the addition of short fibers into FDM materials to increase the part strength. Zhong et al. found that with additional preparation, ABS impregnated with short, reinforcing fibers can be used in FDM [14]. Using a similar idea, the work of Shofner et al. revealed that the addition of these fiber increases stiffness and strength of FDM parts [15].

While such work is essential to the transformation of FDM into an RM process, composite and FEA analyses are limited by the accuracy of the directional properties for a given material. These properties are derived from bonding strength, which is predicted via the thermal and bonding models. As such, correctly predicting inter-filament bonding is critical. The current work therefore seeks to improve previous modeling efforts by including the temperature dependence of material properties in the cooling and bonding models. By considering the change in thermal properties throughout the cooling process after a filament is deposited, a more accurate model is created, providing a better foundation for the prediction of the behaviors of whole parts.

Another factor inhibiting FDM from becoming an RM process is the part weakness along the axis that is perpindicular to the deposition layers (the z-axis). Some aerospace industry leaders claim to have experienced a loss of up to 30% in tensile strength along this axis [16]. Clearly, such a reduction in part strength is a design limitation, either reducing the variety of applications in which FDM parts can be used or requiring additional material to compensate for the reduction of tensile strength. As such, the current work investigates the effects of process parameters on

the z-axis strength and seeks to improve bonding in the z-direction through an annealing post-processing treatment.

For FDM to become an RM process, the models used to predict the bonding between filaments must become more accurate, such that the directional properties of a given material are correct when used in either classical laminate theory or FEA. The weakness in the z-axis must also be understood and improved, if possible, in order to reduce the design limitation that it currently presents. Proper modeling leading to the prediction of part behavior and progress towards more isotropic part behavior are critical to the improvement of FDM such that it can be used as an RM process.

2. Investigation Approach

In order to develop the predictive model, the process physics and their effect must be investigated and understood, beginning with fabrication and progressing through to the application of an FDM part. Tracing backwards from a final part then reveals the appropriate path for the current work. The strength of a part fabricated by FDM is derived from its shape and the orientation of its layers and filaments, the filaments often being approximated as the fibers of a composite structure. Because much work has already been done in the area of developing analytical and numerical methods to predict the strength of both homogenous and composite structures, macro-scale prediction of part behavior is not addressed in this work. Continuing with the analysis of FDM part strength, the aforementioned layers derive their strength from the bonding that occurs between filaments. Because the inter-filament bonding is primarily driven by molecular diffusion and diffusion is a temperature-dependent function,

the heat transfer process experienced by each filament as it is deposited from the liquefier nozzle has a direct impact on bonding, which contributes to the final part strength. Therefore, the cooling process that each filament undergoes serves as the logical beginning for a predictive model.

The cooling profile for a given FDM filament is found using analytical equations describing the heat transfer from the filament to the surrounding environment, which occurs via conduction and convection. While previous work has accomplished simplified cooling models, the current work includes the temperature-dependence of material properties such as specific heat capacity and thermal conductivity, increasing the accuracy of the cooling model. After achieving the thermal history of a filament, the temperature data is used to determine the bonding between adjacent filaments. The bonding equation is a differential equation solved using a 4^{th} order Runge-Kutta method. This equation is a function of temperature (calculated from the cooling model), surface tension, and viscosity. Again, the current work improves upon previous research by including the variability of viscosity with respect to temperature. Note that the temperature-dependence of surface tension was not considered as neither lab used to obtain material properties included surface tension in the experimental battery. Note also that the surface tension value used for Ultem is approximated by using the surface tension of PC, a major constituent of Ultem. This is due to the fact that a true value for Ultem was not available because of intellectual property considerations.

To validate the cooling and bonding models, sample parts were built from polyphenylsulfone (PPSF) according to the experimental matrix shown in Table 2.1 (the table includes repetitions of varied experiments because it is a reduced form of a L9 Taguchi matrix). PPSF was selected as a

material of interest due to its extremely favorable toughness, impact resistance, and natural flame retarding properties [17, 18]. PPSF can also be fabricated in a transparent or colorable form, making it an ideal option for parts with visible surfaces.

Table 2.1. Experimental matrix for model validation

Experiment No.	Extrusion Temperature (K)	Oven Temperature (K)
1	673	498
2	673	498
3	673	503
4	678	498
5	678	498
6	678	503
7	683	498
8	683	498
9	683	503

The parameters in Table 2.1 were used to build samples with a single bond in the z-axis. The single z-bond parts serve multiple purposes: 1) to provide a simple, one-dimensional verification of the combined cooling and bonding models, 2) to produce a correlation between bond length and bond strength and 3) to allow for further investigation into the mechanism affecting the current z-axis strength exhibited in FDM parts (the final objective being a direct request from the author's sponsor as z-axis weakness is a significantly inhibiting factor in using FDM parts in

fully-functional service capacities). In order to avoid warping such a thin, fragile specimen, the parts were built in a self-supporting “square tube”, shown in Fig. 2.1.

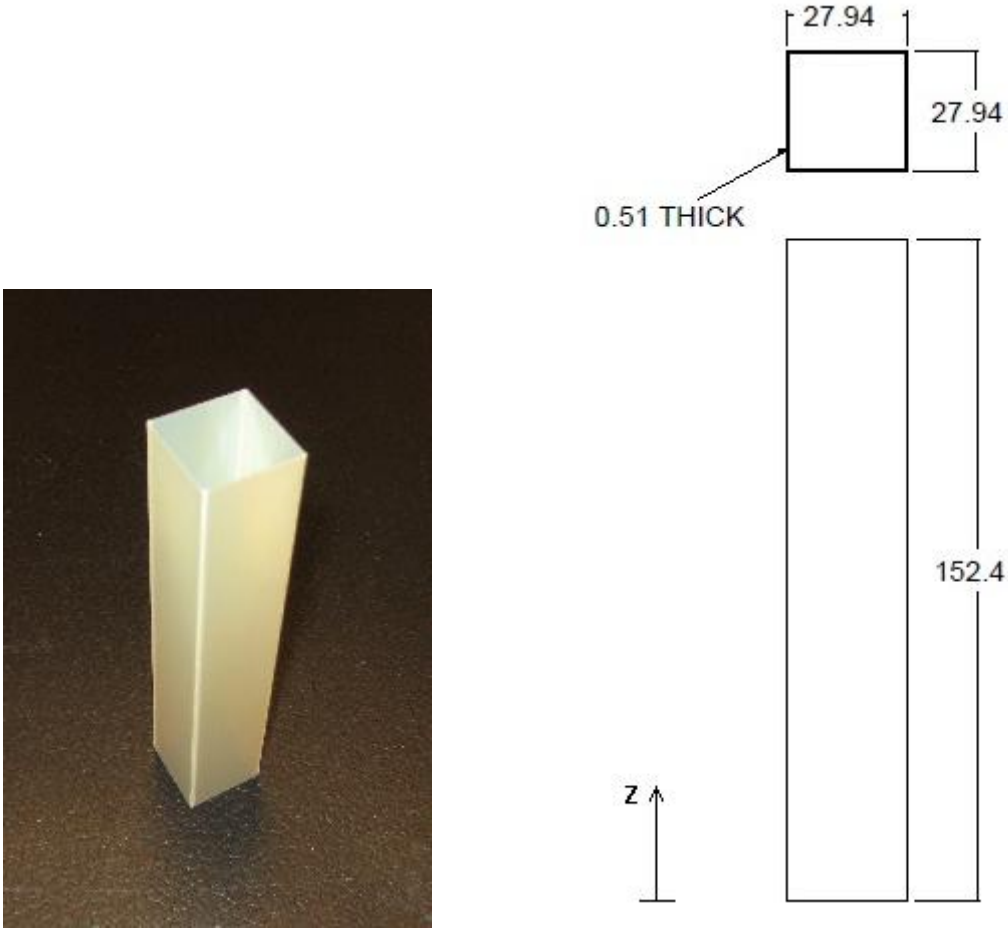

Fig. 2.1. The self-supporting “square tube” configuration of single z-axis bond specimens.

The tubes were then separated into individual specimens and were used in a standard “mini” tensile test. The failure loads measured during these tests were correlated to the predicted bond lengths to characterize trends and derive a relationship between bond length and bond strength.

Following the tensile tests, samples were taken from each of the nine experiments and magnified with a scanning electron microscope (SEM). The resulting images were then imported into ImageJ, a freeware program used for image analysis. Using ImageJ, the bond lengths were measured and compared to the predicted bond lengths to verify the accuracy of the cooling and bonding models.

After verifying the predicted bond lengths, experimentation was conducted to investigate the possibility of improving bond length and/or bond strength through post-processing (annealing). These experiments were conducted with specimens fabricated from Ultem 9085 (henceforth referred to only as Ultem) according to the experimental design in Table 2.2. Ultem was another material chosen for this study because of its appeal in the aerospace industry due to its FAA compliant heat release potential [19]. This property ensures the safety of passengers on an aircraft in the event that Ultem parts catch fire. This polymer is a new material created by blending polyetherimide (PEI) with polycarbonate (PC). The resulting plastic, like PPSF, shows superior flame retarding properties and ductility [20]. Ultem also has high melt flow stability, which is ideal for the FDM process [20].

Table 2.2. Annealing experimental table.

Experiment	Baking Temp (K)	Baking Time (min)
1	409	15
2	364	25
3	364	5
4	455	5
5	455	25
6	409	29
7	409	11
8	473	15
9	345	15

After annealing, SEM images were obtained of the post-processed samples and the bond lengths were compared to the original predicted bond lengths to determine whether or not bond length increased. Miniature tensile tests were then conducted once more to correlate bond length to bond strength.

Through the use of cooling and bonding models, the bond lengths of an FDM part can be predicted based upon the part's fabrication parameters with moderate success. The bond lengths can then be used to calculate the resultant strength of the individual bonds in part. The predictive model, therefore, provides the critical first step in a holistic model that will allow the design engineer to determine the appropriate design for a given part without the need for

excessive experimentation, improving both cost and time efficiency. This, in addition to the investigation of improving bond length through annealing make the current work a valuable resource in the continuing effort to evolve FDM into an RM process.

3. Modeling

3.1 Thermal Model

Because the bonding between adjacent filaments in the FDM process is primarily driven by molecular diffusion, and because molecular diffusion is a temperature dependent process, it is necessary to know the thermal history of an extruded filament in order to predict the bonding that will occur between that filament and an adjacent one. Several factors affect the heat transfer from a filament to its surrounding environment and to an adjacent filament. Filament geometry, material properties, and the convective heat transfer coefficient all influence cooling and therefore must be defined before calculating the temperature profile.

3.1.1 Filament Geometry

The significance of filament geometry in cooling is derived from the fact that convective heat transfer is highly dependent on the shape and exposed area of the thermal mass. Thus, area

and perimeter are important definitions for the cooling model. These parameters, as defined by Bellehumeur et al. [8], are given by

$$A = \pi ab \tag{3.1}$$

$$P = \pi(a + b)\left(\frac{64-3\lambda^4}{64-16\lambda^2}\right) \tag{3.2}$$

in which λ is further defined as

$$\lambda = \frac{a-b}{a+b} \tag{3.3}$$

Additionally, *a* and *b* are the major and minor axes, respectively, of the approximate elliptical shape of a deposited filament, as shown in Fig. 3.1. The values for these axes are 0.254 mm and 0.548 mm, respectively for this study.

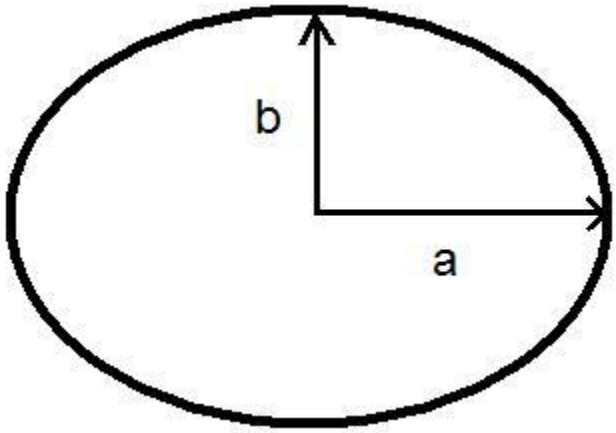

Fig. 3.1 Graphical representation of the elliptical shape of a deposited filament

Using the mathematical definitions for the filament geometry, the heat transfer equation can be better understood.

3.1.2 Cooling Equation

The equation used to calculate the cooling profile of an FDM filament is a simplified, one-dimensional heat transfer model, taken from the work of Bellehumeur et al. [8] and based upon the assumption that the behavior of the cross-sectional area of a filament can be modeled by lumped-capacitance as

$$\boldsymbol{T = T_\infty + (T_o - T_\infty)e^{-mt}} \tag{3.4}$$

in which T is the filament temperature, T_∞ is the oven temperature, T_o is the extrusion temperature, t is time, and m is further described by

$$\boldsymbol{m = \frac{\sqrt{1+4\alpha\beta}-1}{2\alpha}} \tag{3.5}$$

The parameters α and β are functions of both material properties and the geometry of the filament. These parameters are defined as

$$\boldsymbol{\propto = \frac{k}{\rho C}} \tag{3.6}$$

$$\boldsymbol{\beta = \frac{hP}{\rho CA}} \tag{3.7}$$

where k is thermal conductivity, ρ is density, C is thermal heat capacity, and h is the convective heat transfer coefficient. The area and perimeter (A and P) have already been established. As mentioned previously, the current work improves upon previous research by including the temperature dependence of material properties. This topic, as well as the convective heat transfer coefficient is addressed independently for clarity.

3.1.3 Temperature Dependent Material Properties

To effectively address the temperature dependence of the thermal conductivity and specific heat capacity, discrete values of material properties across a range of temperatures were obtained from DatapointLabs for PPSF [21] and from The Boeing Company for Ultem [22]. These values were then fit with appropriate relationship for PPSF and Ultem, shown in Fig. 3.2-Fig. 3.5 (for raw data see Appendix A).

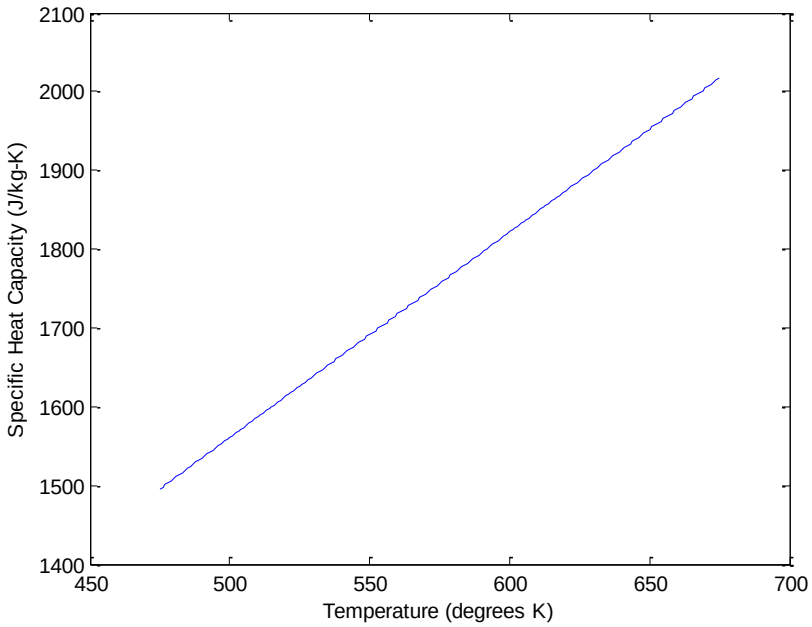

Fig. 3.2. Linear relationship between specific heat capacity and temperature (PPSF).

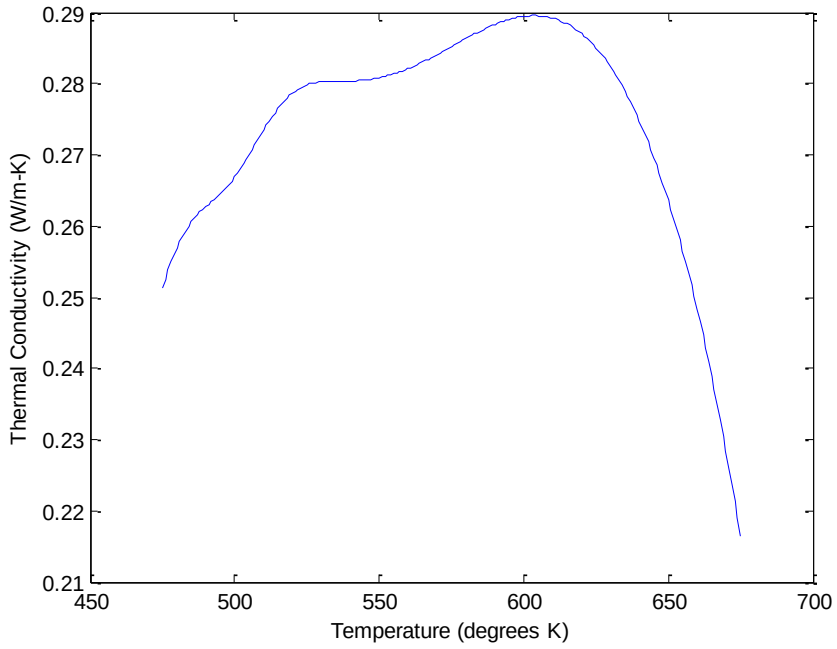

Fig. 3.3. Spline fit showing the temperature dependence of thermal conductivity (PPSF)

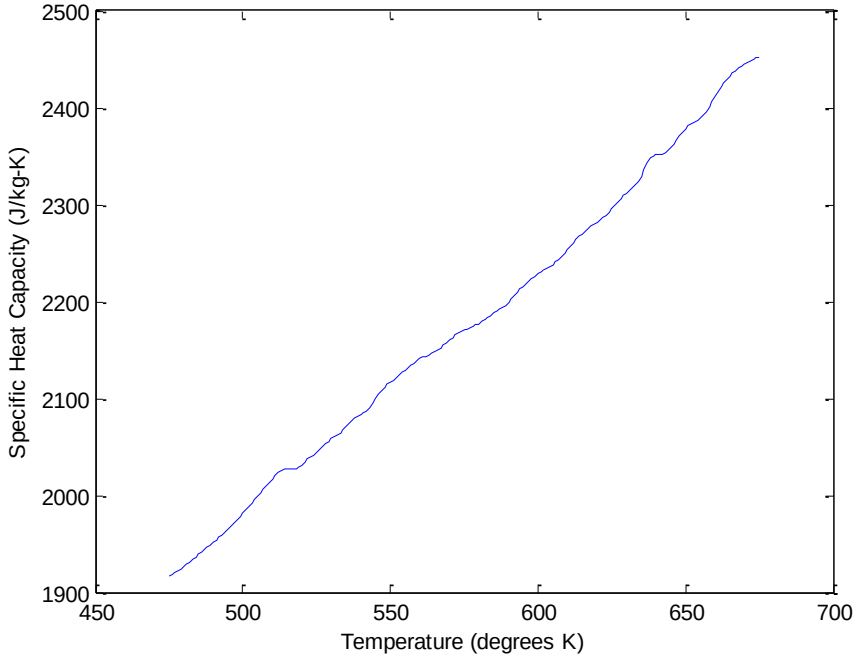

Fig. 3.4 Spline fit showing the temperature dependence of specific heat capacity (Ultem)

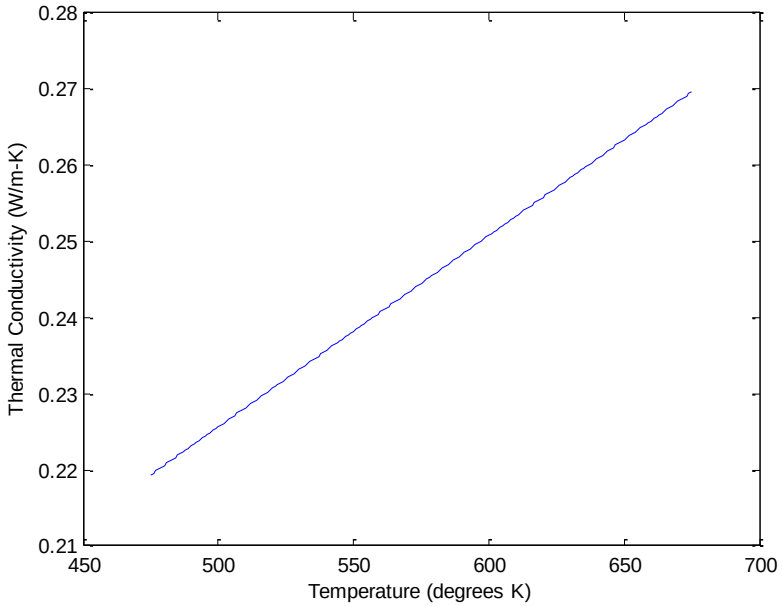

Fig. 3.5 Linear relationship between temperature and thermal conductivity (Ultem).

The above relationships allow the cooling model to use the interpolated material property values at each time step, improving the accuracy of the model over previous works that used constant material properties.

3.1.4 Convection Heat Transfer Coefficient

The convection heat transfer coefficient, *h*, was calculated by modeling the FDM filament as a horizontal cylinder experiencing free convection. Free convection is used because the air flow inside of the build oven is minimal. Conduction is neglected under the lumped capacitance assumption and therefore a single heat transfer coefficient is used for the entire boundary of the filament. This heat transfer coefficient is found using the Nusselt number

$$\boldsymbol{Nu = \frac{hD}{k}} \tag{3.8}$$

in which *D*, the equivalent diameter of the filament, is described as

$$\boldsymbol{D = \frac{4A}{P}} \tag{3.9}$$

where *A* and *P* have been previously defined in Eqs. 3.1 and 3.2. The convection coefficient can be found solving the Nusselt number for *h*. However, this requires a known value for the Nusselt number. This value is derived from a correlation for the aforementioned horizontal cylinder experiencing free convection, given by

$$\boldsymbol{Nu = \left\{ \sqrt{Nu_o} + \left[\frac{\frac{GrPr}{300}}{\left(1+\left(\frac{0.5}{Pr}\right)^{9/16}\right)^{16/9}} \right]^{1/6} \right\}^2} \tag{3.10}$$

where Nu_o=0.36 (a constant value for this Nusselt correlation), *Pr* is the Prandtl number, and *Gr* is the Grashof number, which is defined as

$$\boldsymbol{Gr = \frac{g\beta(T_s - T_\infty)D^3}{v^2}} \tag{3.11}$$

in which *g* is gravity, *β* is the volumetric thermal expansion coefficient, *D* is the diameter of the object being cooled (using the definition from Eq. 3.9, and *v* is the kinematic viscosity. Note that while the *Pr*, *β*, and *v* are all properties of air that vary with temperature, these values are well established and documented. As such, the temperature-dependent relationships for these parameters are not belabored here and are found instead in Appendix B.

Thus, Eqs. 3.1-3.11 are used in an iterative, fixed-time step m-file (*d1_cooling.m*, see Appendix C) to calculate the temperature of an FDM filament as it cools in the fabrication oven. The m-

file re-calculates temperature dependent properties of both air and the polymer being investigated to obtain an improved solution for the simplified, 1-dimensional heat transfer analysis.

3.2 Bonding Model

As previously discussed, the strength of an FDM part is derived from the strength of its bonds between filaments, both within an individual layer and between layers. The strength of individual bonds is directly correlated to the length of the bond between participating filaments. Therefore, in order to develop a model that will predict end part behavior, it is necessary to be able to accurately predict the bonding that occurs between FDM filaments during the fabrication process.

3.2.1 Bonding Equation

The prediction of bonding between filaments is accomplished using a modified form of Frenkel's model for sintering from the work of Pokluda et al. [9]:

$$\theta' = \frac{\Gamma}{a_o \eta} \frac{2^{-5/3} cos\theta sin\theta (2 - cos\theta)^{1/3}}{(1 - cos\theta)(1 + cos\theta)^{1/3}} \tag{3.12}$$

where Γ is the material surface tension and η is viscosity, which is temperature dependent. Again, for clarity, the temperature-viscosity relationship will be addressed independently. Both

ϑ and a_o are geometric parameters, with θ being the bond angle and a_o being the initial radius of a cylindrical filament depicted graphically in Fig. 3.6.

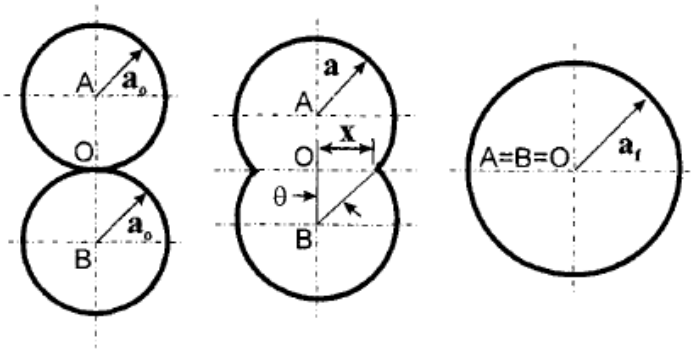

Fig. 3.6 Visual representation of filament geometry for the bonding model [9].

Note that because FDM filaments are elliptical, a_o is considered to be the *equivalent* radius of the previously described ellipse. Note also that Eq. 3.12 is a differential equation, requiring the initial condition:

$$\boldsymbol{\theta(t) = \left(\frac{t\Gamma}{\eta a_o}\right)^{1/2}} \tag{3.13}$$

Inspecting Eq. 3.13 [9], it is seen that the solution must be initiated at a positive, finite value of time rather than zero to avoid numerical instability. Because Eq. 3.12 is an ordinary differential equation (ODE), it cannot be solved analytically. Using the initial value problem given by Eqs. 3.12 and 3.13, the ODE was solved with a 4th order Runge-Kutta method, according the form:

$$\boldsymbol{\theta_{i+1} = \theta_i + \frac{1}{6}\Delta t(k_1 + 2k_2 + 2k_3 + k_4)} \tag{3.14}$$

$$\boldsymbol{t_{i+1} = t_i + \Delta t} \tag{3.15}$$

where Δt is the time-step used, and the k values are further defined as

$$\boldsymbol{k_1 = f(t_i, \theta_i)} \tag{3.16}$$

$$\boldsymbol{k_2 = f\left(t_i + \frac{1}{2}\Delta t, \theta_i + \frac{1}{2}\Delta t k_1\right)} \tag{3.17}$$

$$\boldsymbol{k_3 = f\left(t_i + \frac{1}{2}\Delta t, \theta_i + \frac{1}{2}\Delta t k_2\right)} \tag{3.18}$$

$$\boldsymbol{k_4 = f(t_i + \Delta t, \theta_i + \Delta t k_3)} \tag{3.19}$$

Thus, the bonding angle, and therefore the bond length, between filaments can be predicted. Note that the bonding equation itself lacks any temperature terms and is therefore not an explicit function of temperature. The correlation with temperature occurs in the form of temperature-dependent material properties, similar to the cooling model.

3.2.2 Temperature Dependent Viscosity

A brief inspection of Eqs. 3.12 and 3.13 reveals an apparent time-dependent function. Under the assumption of constant material properties, the bonding equations are indeed only a function of time, which, in fact, negates the necessity of a cooling profile in order to predict bond length. However, viscosity, which is relevant to bonding, is temperature-dependent. The motive for including temperature-variant properties in the bonding model is the same as the cooling model: to improve upon previous work by refining the models used and providing more accurate results.

While line and spline fits were used in handling the material properties relevant to the thermal model, the behavior of viscosity was more readily addressed using interpolation (more

specifically, the built-in MATLAB function *interp1*). The results of these interpolations are shown in Fig. 3.7 and Fig. 3.8.

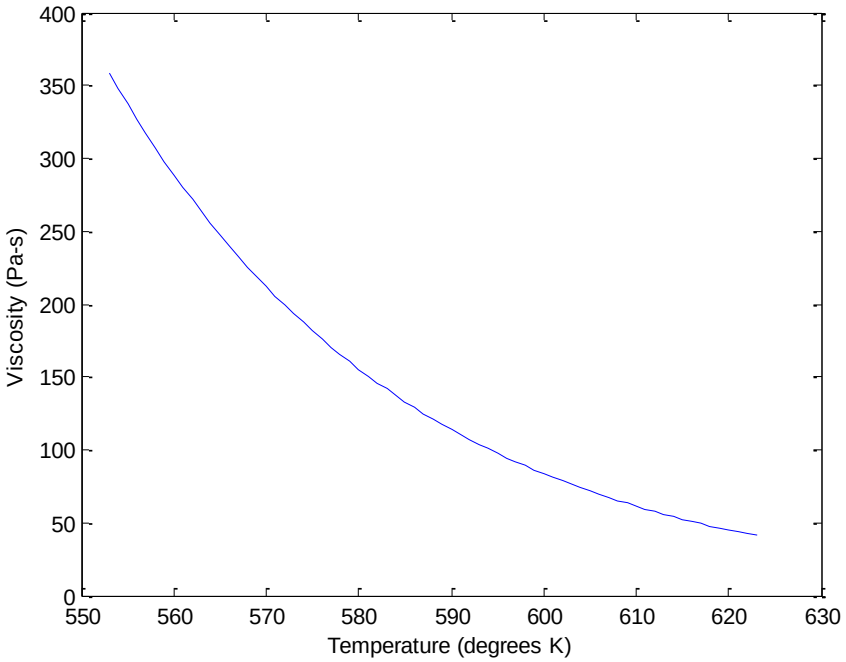

Fig. 3.7. Plot showing the exponential fit used for viscosity (PPSF).

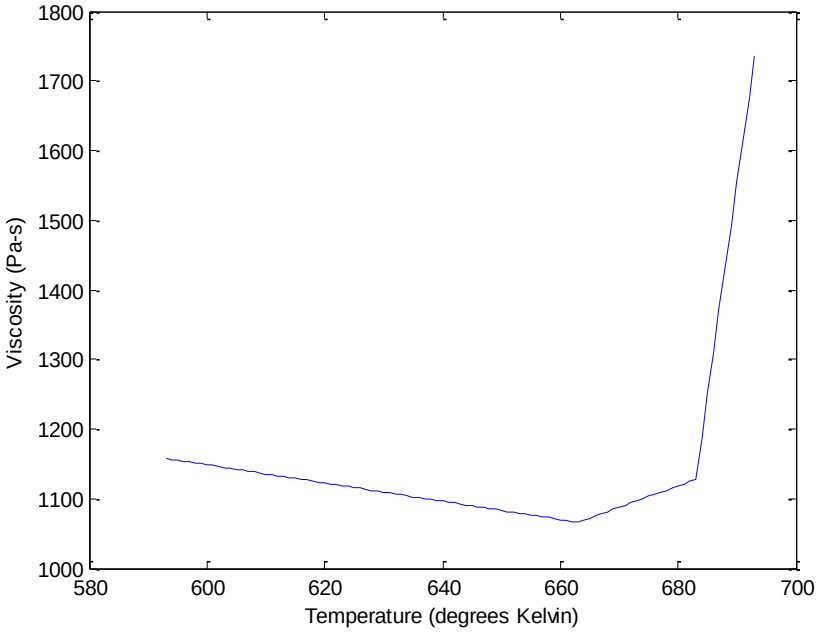

Fig. 3.8. Plot showing spline interpolation of viscosity for (Ultem).

The use of temperature dependence in viscosity alters the bonding equation to become a function of temperature as well as time, connecting the significant physics that relate to bond length, which in turn lead to bond and part strength. Thus, combining the cooling and bonding models completes the prediction of part behavior with regard to heat transfer and polymeric sintering. The predictions of these bond lengths, based upon the fabrication parameters, are validated through SEM images and correlated to the tensile strength of the bonds with miniature tensile tests.

4. Miniature Tensile Tests

4.1 Testing Equipment

While most tensile tests at the University of Missouri-Columbia are completed using the MTS tensile test machine, this machine is not suitable for the miniature tensile tests required by the present work. The grippers used are far too powerful and it is difficult to find a load cell with a small enough range so as to be sensitive and accurate in measuring the relatively low tensile strength of single FDM bonds. To accommodate the needs of the research, a miniature tensile test machine (shown in Fig. 4.1) was built in-house.

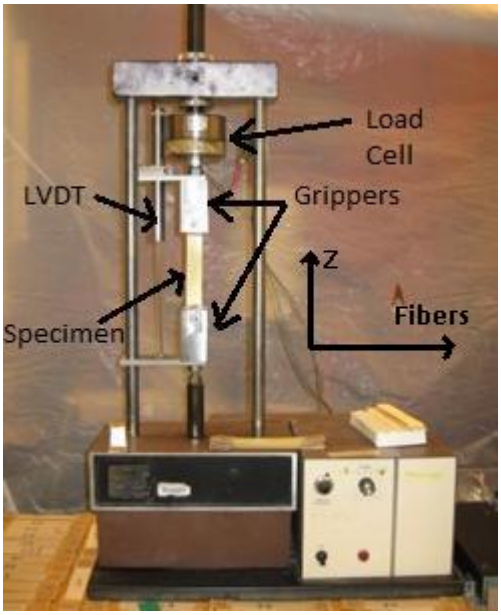

Fig. 4.1. Miniature tensile test machine built to test single-bond specimens.

The tensile specimen is held by two mechanical grippers, which both rotate on the pulling axis and move linearly fore and aft in the plane of view in Fig. 4.1. The movement of the grippers

allows for adjustment independent of one another to ensure that the tensile specimen is properly loaded throughout the test.

The miniature tensile test machine measures both load and displacement through a 500 lb. load cell and a linear voltage displacement transducer (LVDT). Both the load cell and LVDT are connected to a data acquisition system. This system sends the resultant voltage signals to LabView 7 Express on the lab computer, where the signals are both plotted and stored. The data is then imported into Microsoft Excel for analysis.

4.2 Testing Method

4.2.1 Sample Preparation

Because the miniature tensile specimens are comprised of single bonds in along the z-axis, they are very thin, and therefore fragile. As previously mentioned, this fragility prevents the specimens from being fabricated in a form that can be readily tested. The tensile bars must therefore be removed from the square tube structure used in fabrication (ref. Fig. 2.1) to prepare them for testing.

The method for removing the tensile specimens from the original square tube is fairly short and simple. To start, a wooden “template” was created, slightly smaller in width than the square tubes. This template serves to support the tube as it is being cut. The additional support aids in avoiding tearing the specimens, as bonded FDM filaments, especially those singly bonded along the z-axis, are extremely weak in shear. After inserting the template, the square tube is cut

along one of its edges with a razor blade. A specimen with the inserted template is shown in Fig. 4.2.

Fig. 4.2. The supportive wooden template used to assist in specimen removal.

The cutting process is repeated four times for each square tube. Because removing the specimens by cutting with a razor blade is not an extremely precise process, two sections from each tube are unusable, leaving two usable sections with extra material that needs to be removed, as seen in Fig. 4.3.

Fig. 4.3. A usable, but unfinished specimen after removal from the original square tube.

Once the additional material is removed, emery paper is adhered to both ends of the specimen. The emery paper increases friction in the mechanical grippers which, in turn, increases grip. Thus, stress concentrations in the gripping region are reduced, producing data based on the true tensile strength of single bonds in the z-direction. After the adhesive is dry, the tensile specimen can be loaded into the miniature tensile test machine and tested.

4.2.2 Procedure

The testing procedure used for the single bonded specimens is very similar to a normal, full-sized tensile test, with the exception that strain is calculated from displacement and original length instead of measured directly with a strain gauge. The use of a strain gauge, while beneficial, is not feasible with the single bonded specimens because the specimens would not be able to support the weight of additional data acquisition apparatuses without significantly altering the test data. With this exception in mind, the testing procedure is as follows:

1) Turn on the miniature tensile test machine and the lab computer.
2) Open LabView 7 Express and load the *mini-tensile test* virtual lab file for data acquisition.
3) Return the miniature tensile test machine to the starting position by turning the directional knob to “retract” and waiting until the machine stops.
4) Load the specimen in the machine, making sure that both the specimen and the grippers are straight so as to not preload in either shear or twisting (see Fig. 4.5 and Fig. 4.6). Tighten the gripper bolts with fingers with the specimen properly oriented (vertical, straight fore/aft, and not preloaded in twisting).

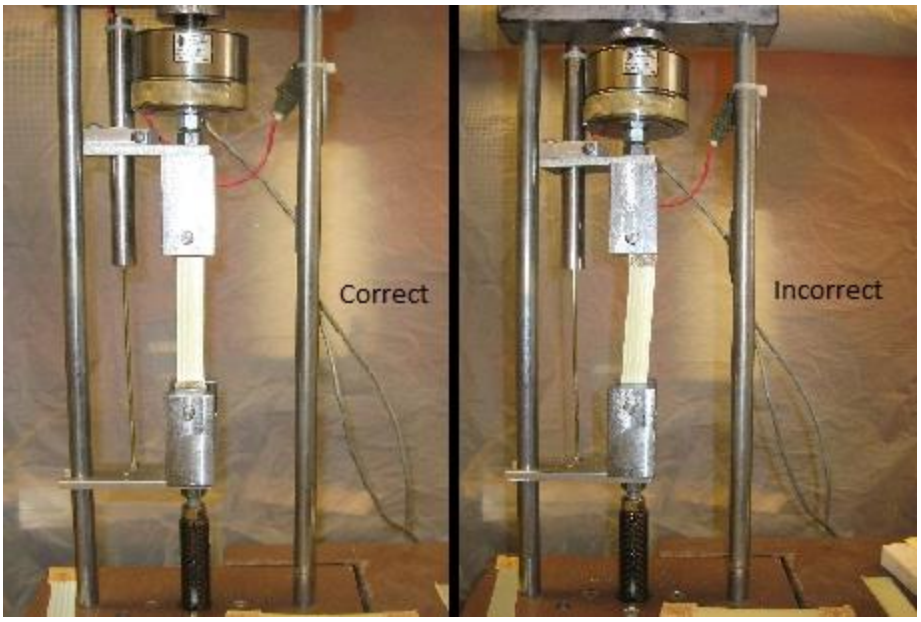

Fig. 4.4. Comparison of properly and poorly loaded specimens in regard to vertical orientation.

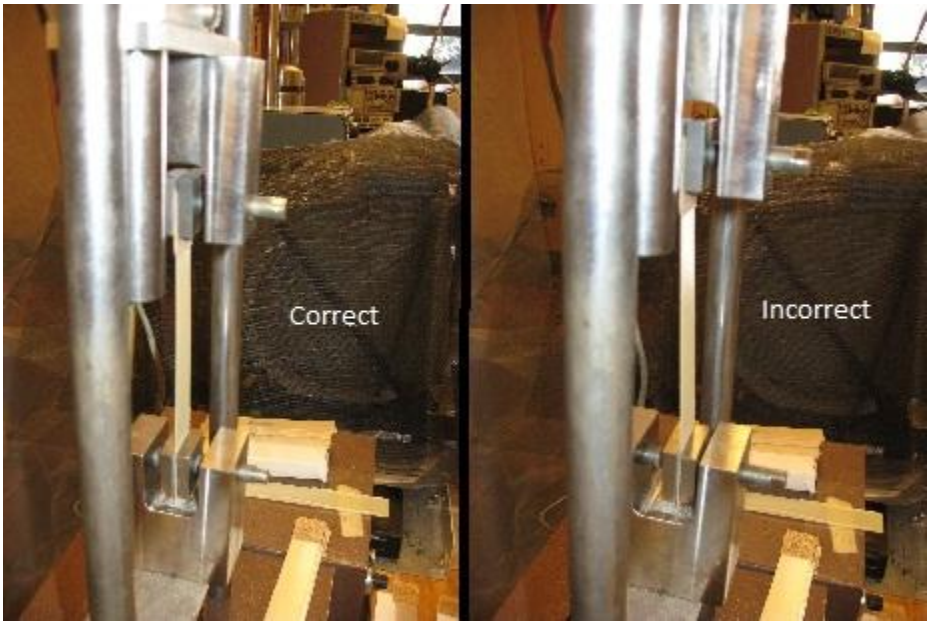

Fig. 4.5. Comparison of properly and poorly loaded specimens in regard to preloading in shear.

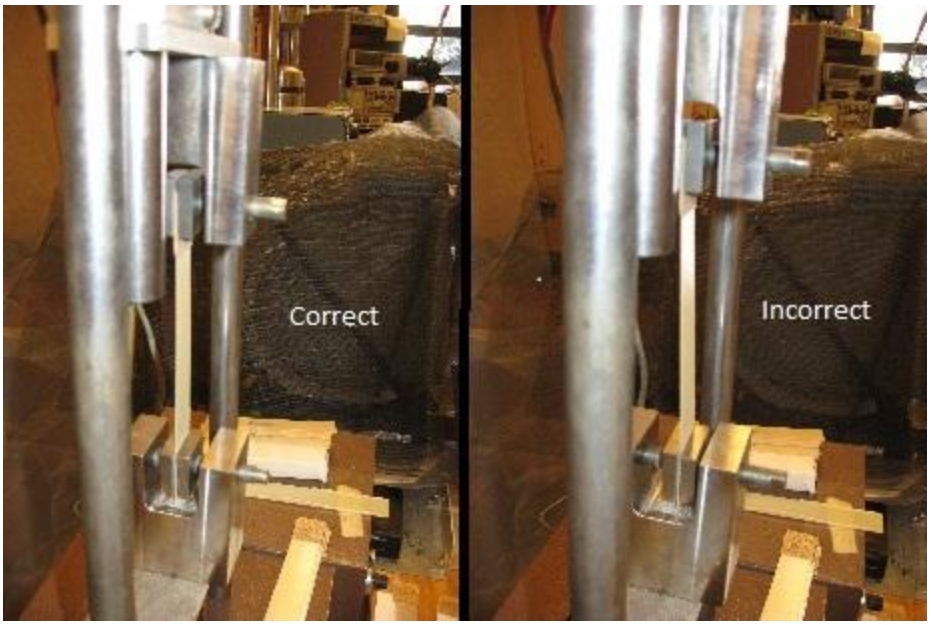

Fig. 4.6. Comparison of properly and poorly loaded specimens in regard to preloading in twist.

5) Tighten the bolts with pliers to ensure that the specimen does not slip in the grippers during the test. Again, verify that the specimen is still vertical and not preloaded in shear or twisting.
6) Start data acquisition by pressing the "play" button in the user interface window of the *mini-tensile test* virtual lab.
7) Turn the directional knob on the test machine to "pull" at a strain rate of 1 mm/min.
8) Pull the specimen in tension until failure.
9) Stop data acquisition via the "stop" button in the virtual lab window.
10) Remove the tensile specimen from the machine.
11) Measure the width of the specimen at the location of fracture. (This is used to determine the fracture area from the measured bond width and predicted/observed bond length. The fracture area is used to calculate maximum stress in the specimen.
12) Repeat steps 3-11 for all specimens in the experimental test battery.

This procedure was used to collect failure data for all of the tensile specimens derived from the experimental matrix given in Table 2.1.

5. Case Studies

5.1 Cooling and Bonding Results

The cooling and bonding models are both equations that result in asymptotic behaviors. The extreme cases for both PPSF and Ultem, as derived from their respective fabrication limits [23], are shown in Fig. 5.1-Fig. 5.8.

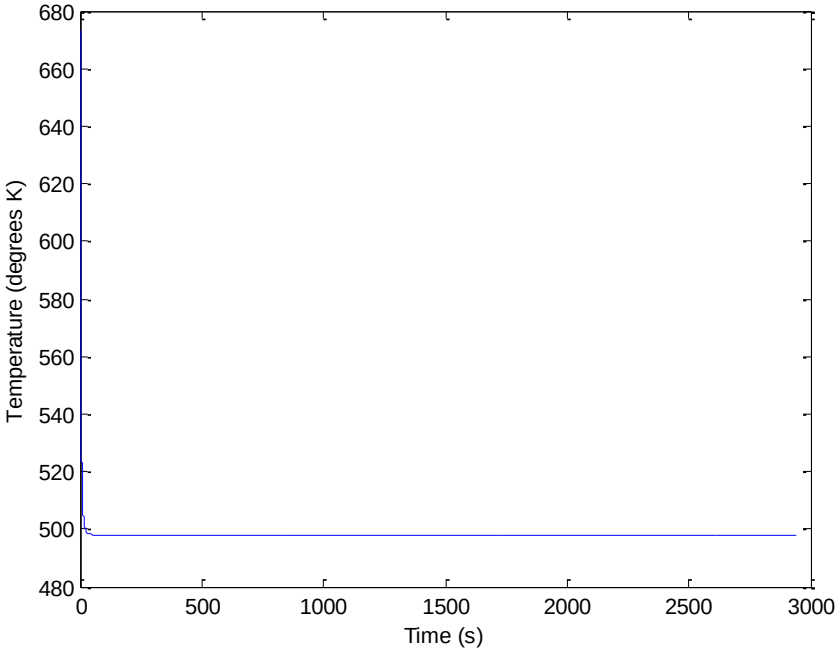

Fig. 5.1. Predicted cooling (PPSF, T_o = 673 K, T_∞ = 498 K).

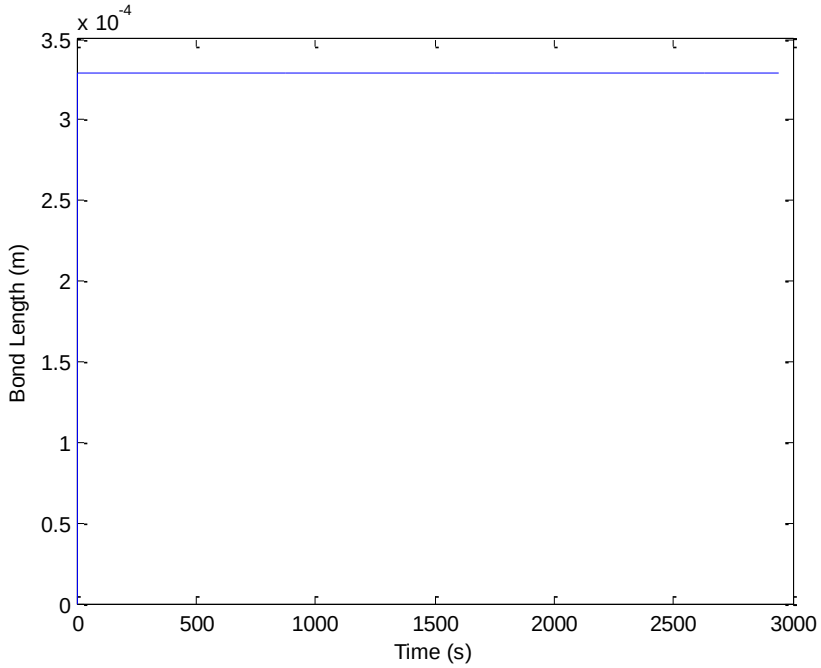

Fig. 5.2. Predicted bonding (PPSF, T_o = 673 K, T_∞ = 498 K).

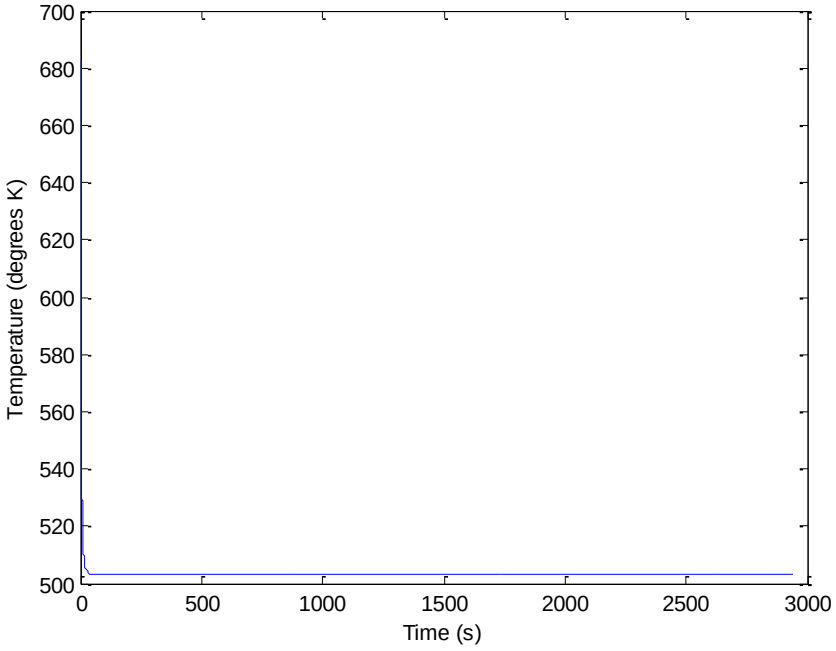

Fig. 5.3. Predicted cooling (PPSF, T_o = 683 K, T_∞ = 503 K).

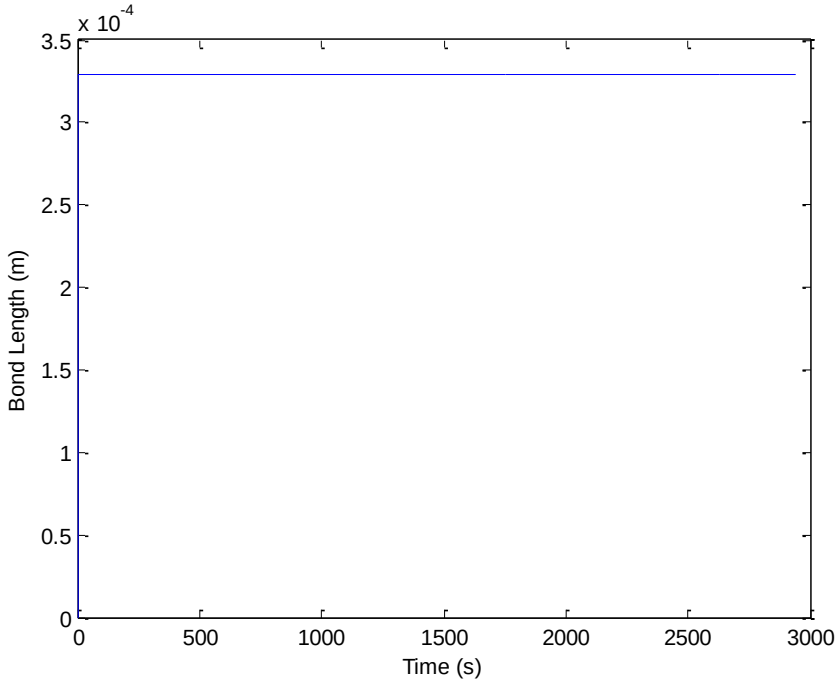

Fig. 5.4. Predicted bonding (PPSF, T_o = 683 K, T_∞ = 503 K).

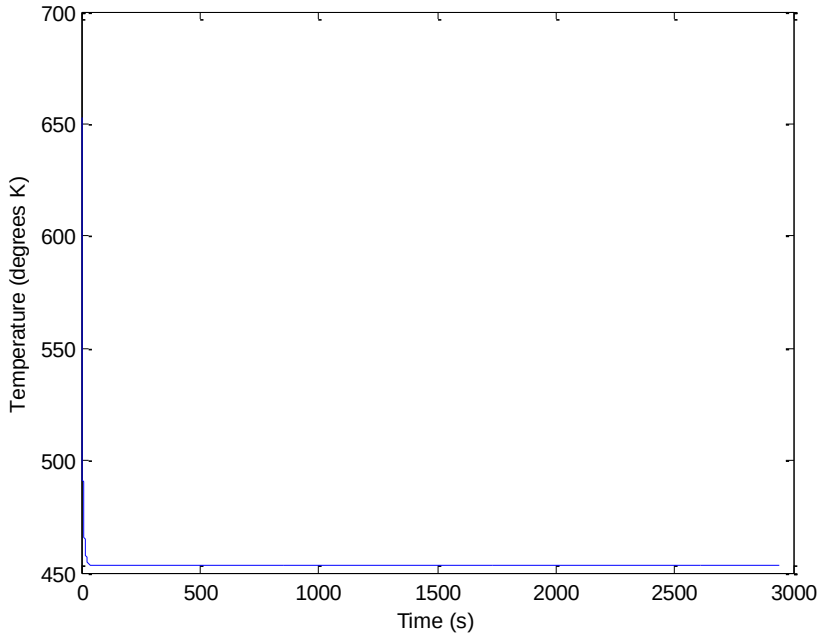

Fig. 5.5. Predicted cooling (Ultem, T_o = 653 K, T_∞ = 453 K).

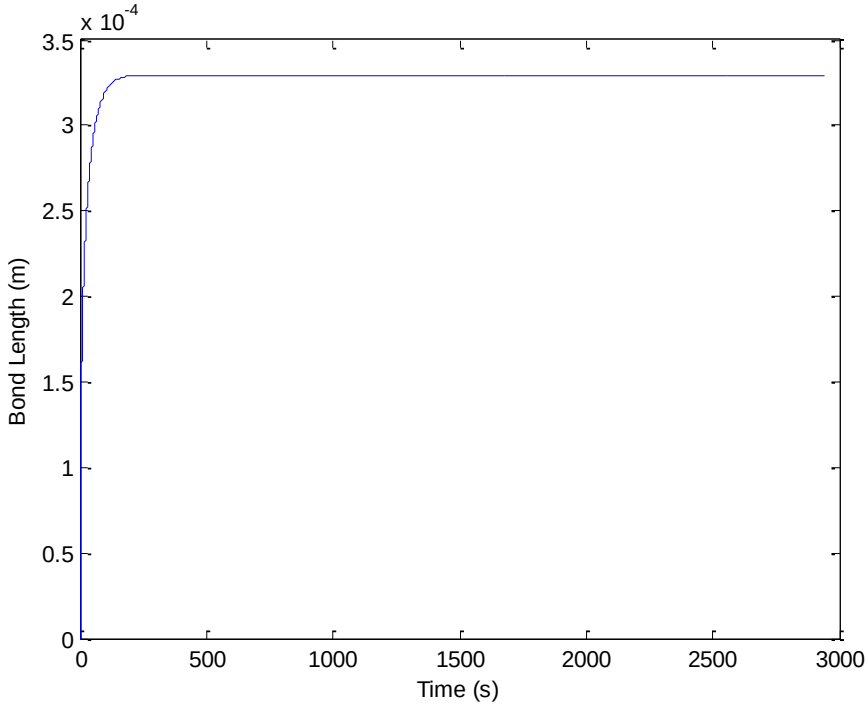

Fig. 5.6. Predicted bonding (Ultem, T_o = 653 K, T_∞ = 453 K).

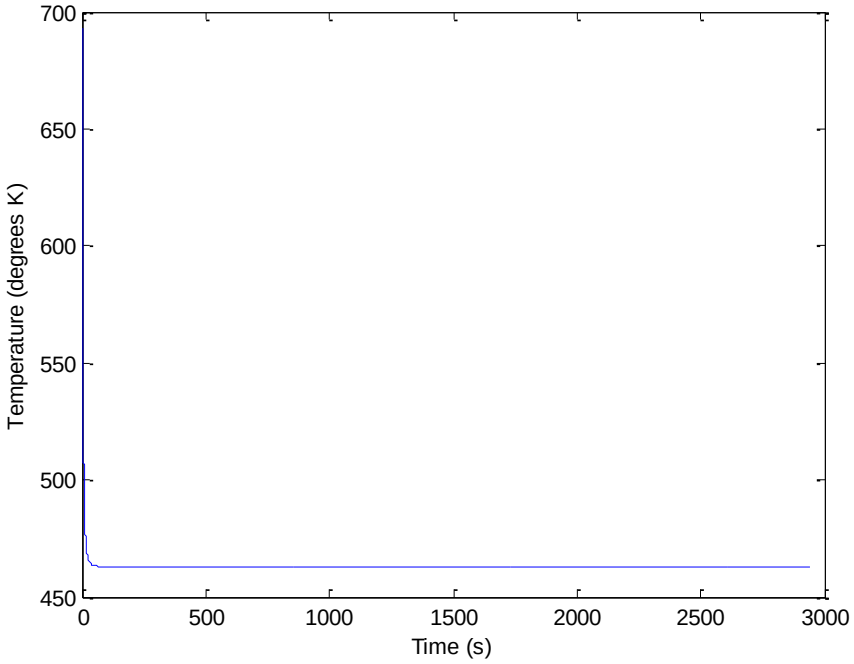

Fig. 5.7. Predicted cooling (Ultem, T_o = 693 K, T_∞ = 463 K).

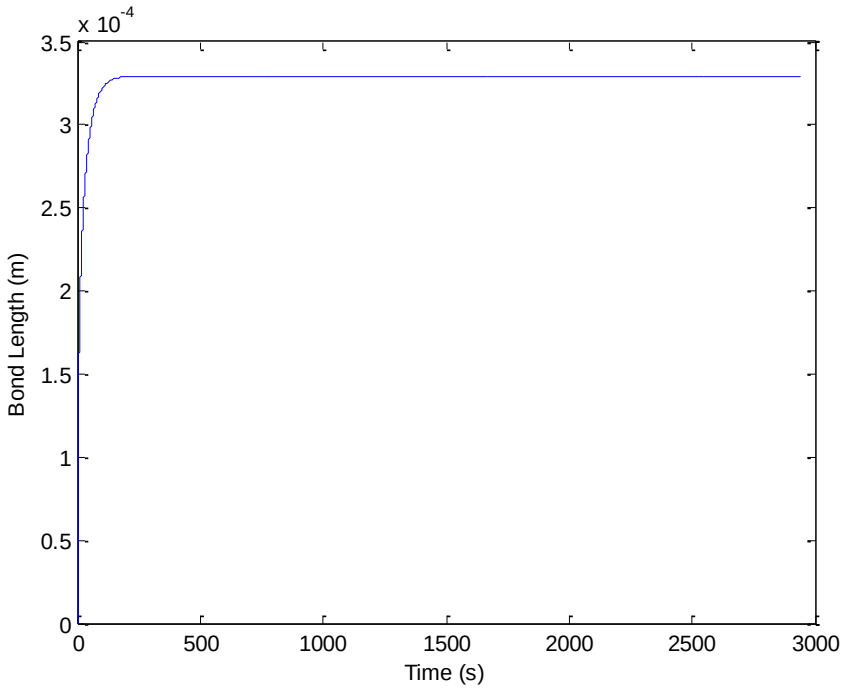

Fig. 5.8. Predicted bonding (Ultem, T_o = 693 K, T_∞ = 463 K).

Note that regardless of the extrusion temperature, oven temperature, and material, steady-state behavior is reached well within the time frame of the initial deposition (about 30-300 s for PPSF and Ultem, respectively. Note that build time for a single square tube is 49 min). Note also that the modeled bond lengths for all cases reach a steady-state value of 0.329 mm. This is because, as determined from a brief inspection of Eq. 3.12 the initial equivalent radius of the bonding filaments serves as the limiting value for a given system as the growth rate of the bond inevitably decays to zero.

5.2 Mesostructure Investigation

The bond lengths between filaments were obtained by analyzing SEM images of the filaments with ImageJ, which is an image analysis software package available for free online. The bond length data from these images were then compared to the calculated bond lengths to determine the validity of the cooling and bonding models.

5.2.1 PPSF

The images shown in Fig. **5.9** and Fig. **5.10** are examples of the mesostructure of PPSF parts created by FDM. Note that only images like Fig. **5.9** were used to validate the predictive model as the model is currently simplified and only considers the case of a single adjacent filament. The comparative analysis of predicted and realized bonding is seen in Table 5.1.

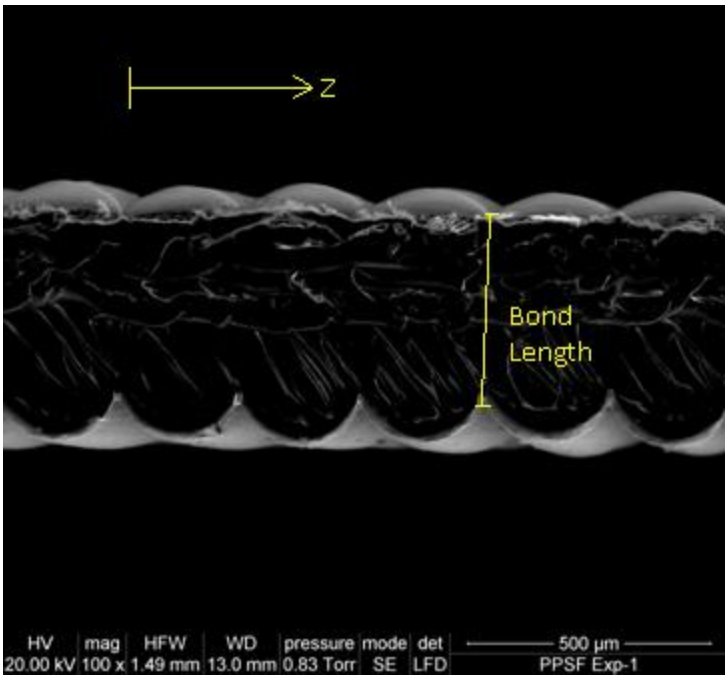

Fig. 5.9. Image of the mesostructure of a miniature tensile specimen (PPSF).

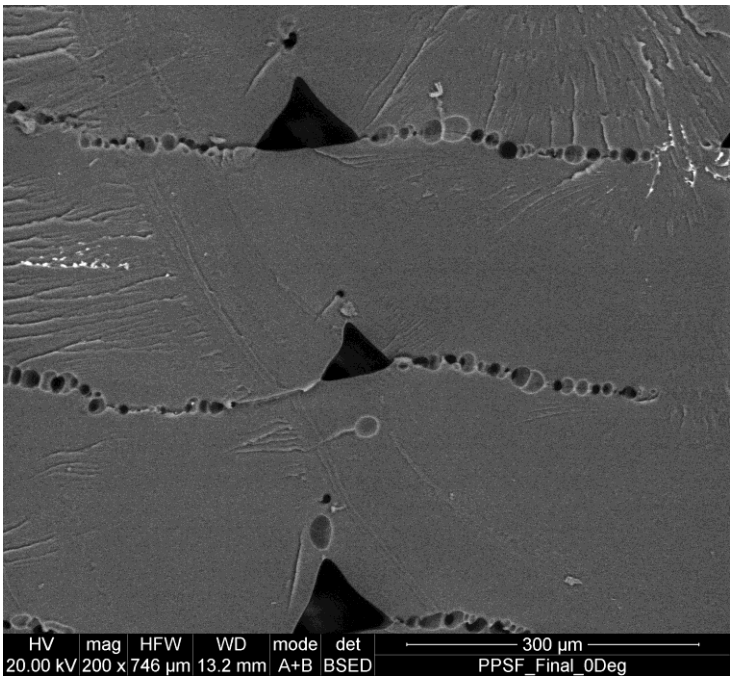

Fig. 5.10. Image of the mesostructure of a full size tensile specimen (PPSF, filaments at 0^{o}).

Table 5.1. Comparison of predicted and actual bond lengths for PPSF

Exp	Predicted (mm)	Observed (mm)	% Error
1	0.329	0.389	15.47
2	0.329	0.354	7.11
3	0.329	0.355	7.19
4	0.329	0.343	4.19
5	0.329	0.413	20.26
6	0.329	0.362	9.02
7	0.329	0.411	20.03
8	0.329	0.409	19.48
9	0.329	0.380	13.33

Table 5.1 shows that the predictive model is accurate within 5% in some cases. However, in other cases the model exhibits over 20% error. All observed bond lengths were greater than the predicted lengths. Also, note the presence of bubbles in the mesostructure of the full-size tensile specimen (Fig. **5**.**10**). These items, while extremely significant, are addressed in the Discussion section (along with their origins and implications) and therefore will not be further belabored here.

5.2.2 Ultem

The images in Fig. **5**.**11** and Fig. **5**.**12** are also pictures of the mesostructure of FDM parts. However, these parts were built from Ultem. Again, bond length data was obtained only from the single-bonded parts. The comparison between predicted and realized bonding is seen in Table 5.2. Note that unlike the PPSF parts, the Ultem parts were post-processed. However, the modeling of the Ultem parts still only considers the original fabrication. This is due to the fact that, according to the model, the original equivalent radius of a filament acts as a limiting factor to final bond length and all predicted bonds reach this limit. Thus, while the possibility of improving bond length and/or strength through "annealing" was investigated, it was not modeled as such calculation would be frivolous. Also, note that the bond lengths in only the extreme cases (least post-processed and most post-processed) were compared to the predicted bonds as the annealing process was found to be detrimental and a full-scale analysis was unnecessary.

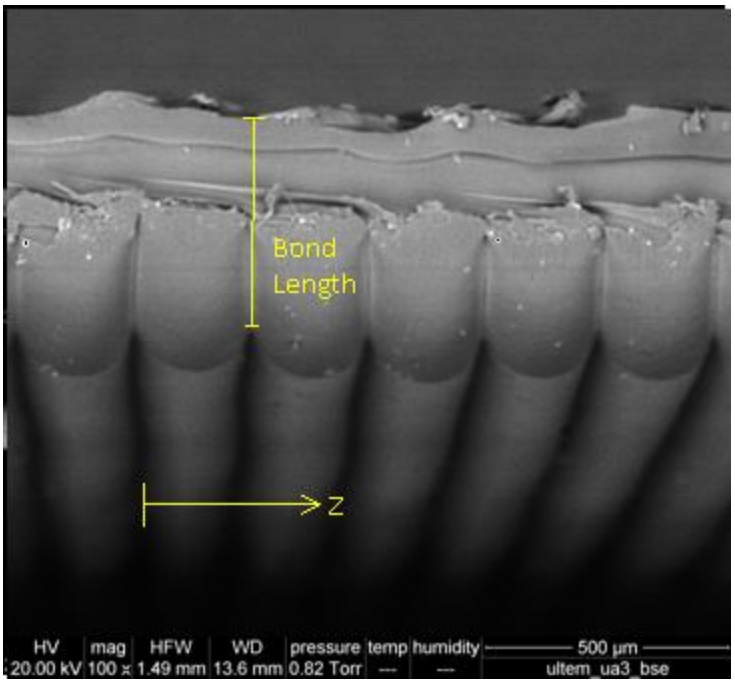

Fig. 5.11. Image of the mesostructure of a miniature tensile specimen (Ultem).

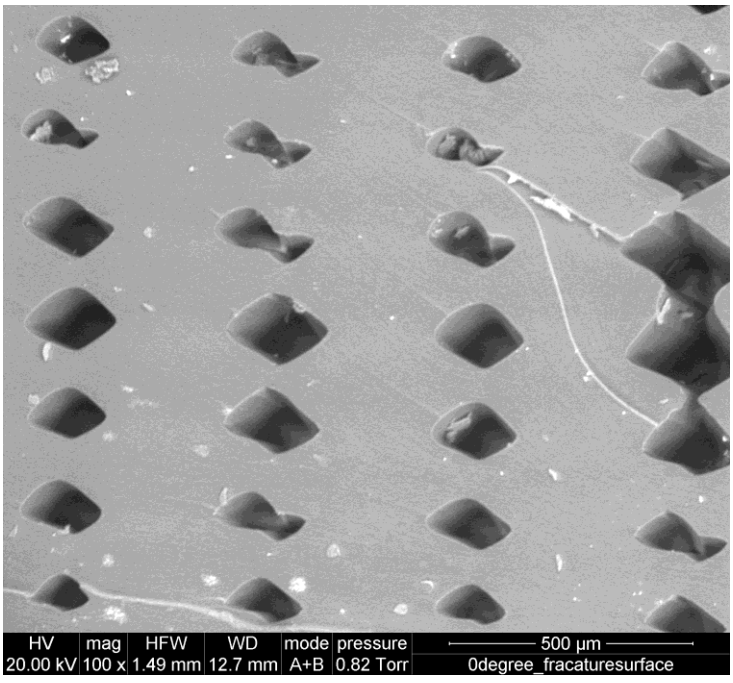

Fig. 5.12. Image of the mesostructure of a full size tensile specimen (Ultem, filaments at 0^{o}).

Table 5.2. Comparison of predicted and actual bond lengths for post-processed Ultem.

Exp	Predicted [mm]	Observed [mm]	% Error
Not Post-processed	0.329	0.351	6.27
3	0.329	0.371	11.32
9	0.329	0.409	19.56

As seen in Table 5.2, the bonding model is reasonably accurate for the Ultem parts that are not annealed. The data shows that the bonding model decreases in precision with increasing amounts of post-processing. Note that the mesostructure of Ultem does not exhibit the micro-bubbles found in PPSF.

5.3 Miniature-tensile Test Specimens

5.3.1 PPSF

The major findings from the PPSF miniature tensile tests are summarized in Table 5.3 and Fig. 5.13. The results indicate brittle fracture behavior as well as revealing the effect of the fabrication parameters on the tensile strength of the miniature tensile specimens.

Table 5.3. Results of miniature tensile tests conducted according to the L9 Taguchi matrix

Experiment	Avg Max Stress (MPa)	Avg Bond Length (mm)	Max % Elongation
1	17.59	0.389	1.133
2	29.12	0.354	1.367
3	15.42	0.355	0.880
4	14.00	0.343	0.622
5	11.22	0.413	0.793
6	13.78	0.362	0.535
7	13.43	0.411	0.725
8	9.80	0.409	0.433
9	14.39	0.380	6.733

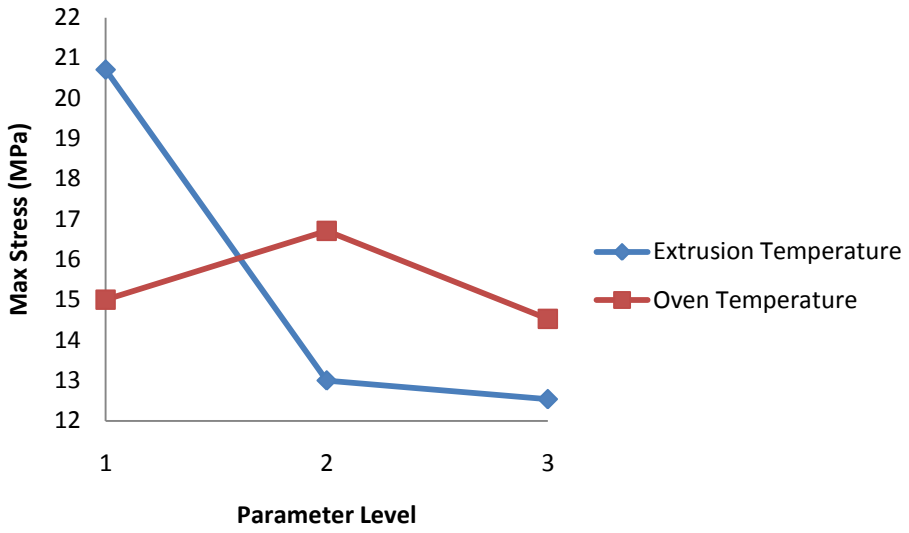

Fig. 5.13. Response plot showing the effect of fabrication parameters on part strength.

The miniature tensile specimens are seen to exhibit tensile strengths between 9.80 and 29.12 MPa, depending on the extrusion and oven temperature during fabrication. The response plot shows a much more severe slope with variance in parameter level for extrusion temperature, meaning that this temperature plays a much more significant role in determining part strength than the oven temperature. This is confirmed by the analysis of variance (ANOVA) that was conducted for this data, which reveals that the extrusion temperature contributes over 94% to the final tensile strength of the miniature tensile specimens fabricated from PPSF (oven temperature contributes the other 6%).

5.3.2 Ultem

The failure loads obtained from the miniature tensile tests are shown in Table 5.4. As previously mentioned and seen from the failure load data, the post-processing has a detrimental effect on tensile strength. Thus, just as only the extreme cases of annealing were investigated via SEM, only the extreme cases were compared to the un-annealed miniature tensile bars in terms of stress. This comparison is shown in Table 5.5.

Table 5.4. Failure loads of post-processed miniature tensile specimens.

Exp	Max Avg Load (N)
Not Post-processed	436.547
1	185.152
2	100.992
3	288.944
4	200.898
5	280.173
6	292.661
7	293.748
8	98.279
9	212.843

Table 5.5. Stress and elongation data for extreme annealing and reference cases.

Exp	Avg Max Stress (Mpa)	Avg Bond Length (mm)	Max % Elongation
Not Post-processed	55.72	0.351	2.363
3	39.92	0.371	1.605
9	24.51	0.409	1.103

Table 5.5 shows that annealing does indeed increase the length of bonds between filaments, but the data set indicates without exception that this type of post-processing reduces maximum failure load, maximum stress, and ductility. Further analysis, such as ANOVA, was deemed unnecessary for this data as annealing proved to be unproductive and undesirable.

6. Discussion

6.1 Cooling and Bonding Models

In general, the cooling and bonding results show common trends for both PPSF and Ultem. A brief review of Table 5.1 and Table 5.2 shows that for both materials, in every case, the predictive bonding/cooling model under-predicts the bond length between adjacent filaments. This numerical is attributed to creep based upon other researchers citing thermal stress as a

significant cause of part deformation [6, 12, 13]. This creep increases bond length via a flattening effect which occurs as subsequent layers are added to an FDM part. With each new layer, additional weight is pressing upon every previous layer, all at elevated temperatures. While creep typically occurs over long periods of time (in materials such as copper or steel pipes), the process is accelerated in an FDM fabrication chamber due to the fact that the oven temperature is very close to the fabrication material's glass transition temperature.

While several factors may play a role in the inaccuracy of the cooling and bonding models, the current work attributes the discrepancy to creep. This is based not only upon the conclusions of previous work, but also on predicted and observed bond lengths of the post-processed tensile specimens. Table 5.2 clearly shows an increase in observed bond length as annealing temperature and time increase. This supports the explanation of creep, for if deformation that increases bond length occurs during normal fabrication due to the weight of previous fabricated layers and increased temperatures, the annealing process, which in some cases was conducted at temperatures higher than the original oven temperature, most certainly accelerates and exacerbates these effects. Fig. **5.11** also supports this explanation. The dark regions that appear between filaments are areas of local thermal stress that were caused during annealing by additional heating and cooling, enhancing the effect of the previously deposited filaments.

Thus, while the cooling and bonding models may accurately predict the bonding process itself, the resultant calculated bond lengths do not accurately reflect the actual bond lengths between filaments in an FDM part. While some researchers have sought to improve the cooling model through considering either 2-dimensional temperature distributions through a filament [7] or multiple thermal contacts from all adjacent filaments [24], this work is limited to predicting the process itself and not the observed resultant bond lengths. As such, in light of the fact that the

purpose of the current work is to serve as an initial step in the achievement of a model that can predict final part behavior, a model for creep would be much more valuable. Though more accurate cooling and bonding models most certainly will be beneficial at some point, they are irrelevant until such a time that creep is either successfully eradicated from the FDM process or predicted through additional modeling. The suggested future work, therefore, is to establish equations for creep and to couple the prediction of creep with the current cooling and bonding models in an attempt to predict not the theoretical bond length, but the realized bond length so that progress can be made towards the goal of an entire process model that will predict final part strength based upon initial fabrication parameters.

6.2 Miniature Tensile Specimens

6.2.1 PPSF

The clearest representation of the trends observed in the miniature tensile tests conducted with PPSF are shown in Fig. 5.13 and Table 5.3. According to the response plot obtained from statistical analysis, both extrusion and oven temperatures play a role in the final z-axis strength of an FDM part, with the extrusion temperature being the more significant of the two. Note that the lower extrusion temperatures actually produce stronger parts. Table 5.3 validates this observation, with the three highest failure stresses belonging to the experiments with the lowest extrusion temperature (cross-reference Table 2.1). This is most likely due to the fact that many polymers experience thermal degradation at high temperatures. PPSF is known to experience thermal degradation by oxidation [25, 26]. Oxidation occurs when free ions bond

with the polymer chain, reconstructing the chemical bonds of the polymer chain. The chemical reconstruction induced by heat reduces the strength of parts fabricated with this material.

The data in Table 5.3 also appears to call into question the assumed relationship between bond length and bond strength, with the greater observed bond lengths actually corresponding to the weakest failure stresses. However, upon inspection of the mesostructure of parts fabricated with PPSF, the seeming debunking of this assumption can be explained. Fig. **5.10** shows several micro-bubbles that formed between filaments during the fabrication process. These bubbles, while obviously reducing the strength of an inter-filament bond, also reduce the effective bond length. Thus, while the apparent bond length may be longer, the bond length that withstands loading may be significantly less. The most likely explanation of the formation of these micro-bubbles is the tendency of PPSF to retain moisture [27], such that during the fabrication process high temperatures cause moisture bubbles to form and prevent proper coalescence between filaments. Whatever the cause, the trend presented by the data renders any attempt at a mathematical correlation between bond length and bond strength useless within the confines of the current work.

The miniature tensile tests conducted with PPSF reveal that thermal degradation and other phenomena resulting from thermal processing (such as the formation of micro-bubbles) are important factors to consider with FDM fabrication. To better understand these effects the investigation described here should be repeated with a larger experimental window to better characterize the effect of extrusion temperature on part strength. Also the mechanism of thermal degradation specific to PPSF and Ultem should be characterized mathematically, if possible, so that its effects can be included in the overall modeling process. Finally, if PPSF is to continue to be used as an FDM material, precautions must be taken to prevent the uptake of

moisture into the polymer to avoid the harmful repercussions of micro-bubbles. Modeling the formation of such bubbles is not suggested as it would be useless. The bubbles are an undesirable trait and should be avoided if possible, unlike creep, which is an inherent aspect of the FDM process.

6.2.2 Ultem

Unlike the PPSF, the main focus of the miniature tensile tests conducted on parts built from Ultem was to determine the effect of annealing instead of characterizing the FDM process itself. While annealing does have the intended result of increasing the bond length (see Table 5.5), it also reduces failure load, failure stress, and ductility. Similar to PPSF, this data appears to contradict the assumed relationship of bond length and bond strength, perhaps proposing that bond length and bond quality are separate considerations. However, Ultem components polyethermide (PEI) and PC have also been to shown experience to thermal degradation, although by different mechanisms [28-31]. Hydrolysis is a phenomenon similar to oxidation, causing a chemical reconstruction through the bonding of free ions to polymer chains. Scission is a much simpler mechanism in which the backbone of the polymer chain breaks at random, reducing molecular weight. Thus, the reduction in strength and ductility exhibited by Ultem is attributed the scission and hydrolysis seen in PC and PEI. Table 5.4 and Table 5.5 both support this logic, with the weaker and more brittle specimens coming from parts that underwent more severe post-processing (cross-reference Table 2.2). The relationship between bond length and bond strength can therefore still be considered a valid assumption. Because the annealing process served only to weaken FDM parts, no further analysis was conducted as it would have

been frivolous. However, the post-processing experiments do serve to again highlight the role of thermal degradation in defining part strength. Thermal degradation is therefore a byproduct that must be understood and minimized before the FDM process and the materials used to build FDM parts can be optimized.

7. Conclusions

While the current work does not claim to provide the final, robust model capable of predicting final part strength, it does providing a beginning effort. The results from the experiments and calculations serve as a formidable guide to the improvement of both future modeling and the FDM process itself. First, the cooling and bonding models were determined to be limited more scope than in accuracy. While assumptions were made to simplify the models, merely refining them is unlikely to improve the accuracy to an extent that would negate the rest of the process physics, such as creep. Avoiding creep altogether is unrealistic in light of the mechanism of the FDM process, and modeling creep deformation, therefore, is a much more productive endeavor for the purpose of achieving a realistic model that can accurately predict bond lengths. The prediction of actual bond lengths, not just theoretical physics, will lead to the eventual prediction of final part behavior and the evolution of FDM into an RM process.

The miniature tensile tests conducted with PPSF tensile specimens reveal that the extrusion temperature is a critical fabrication parameter for z-axis strength. The tests also point to the importance of thermal degradation as an effect of the FDM process that produces undesirable reductions in z-axis strength. Thus, in order to continue to improve the z-axis strength, the experiments described in the current work should be repeated with a larger scope to better

characterize the effect of extrusion temperature on tensile strength. Understanding how to minimize thermal degradation in FDM materials will also help improve z-axis strength, which in turn will improve overall part strength.

Finally, post-processing, at least in the form of annealing, was shown to have only detrimental effects on z-axis strength in parts built from Ultem, despite the increased bond lengths achieved. Again, thermal degradation is the significant contributor to this phenomenon. The conclusion derived for PPSF therefore stands for Ultem as well. Thus, while it is not recommended to further investigate annealing as a means of improving inter-filament bonding, the development of a mathematical description of thermal degradation could prove valuable to an overall process model.

The current work therefore serves to guide future work in the refinement of FDM and the models used to predict parts fabricated with this process. The most promising area for future progress currently lies in FEA, like the work completed by Zhang and Chou [13, 14]. Using the thermal and mechanical modeling capabilities of the ANSYS package, individual mesh elements can be activated in succession to approximate the FDM process. By using the approach presented in this work in a finite-element, which can include both the temperature dependence of material properties and the development of creep (as thermally induced mechanical deformation), it is possible to achieve the predictive ability sought in the current work. This type of modeling, combined with a mathematical characterization of thermal degradation for FDM materials, will result in a process model that can successfully predict the overall strength of FDM parts. In turn, giving design engineers the ability to accurate predict, and therefore design, the behavior of FDM parts will catapult FDM from its current status as an RP process to being an RM process that robust and reliable.

References Cited

1. Fused Deposition Modeling (FDM), custompart.net, Web, May 2010.
2. P. Kulkarni and D. Dutta, Deposition Strategies and Resultant Part Stiffnesses in Layered Manufacturing, *Proceedings of ASME Design Engineering Technical Conferences*, Sacramento, California (1997).
3. B.C. Pennington, N.L. Hoekstra, and J.L. Newcomer, Significant Factors in the Dimensional Accuracy of Fused Deposition Modelling, *Journal of Process Mechanical Engineering*, Vol. 219 (2005), 89-92.
4. B.V. Reddy, N.V. Reddy, and A. Ghosh, Fused Deposition Modelling Using Direct Extrusion, *Virtual and Physical Prototyping*, Vol. 2 (2007), 51-60.
5. Q. Sun, G.M. Rizvi, C.T. Bellehumeur, and P. Gu, Effect of Processing Conditions on the Bonding Quality of FDM Polymer Filaments, *Rapid Prototyping Journal*, Vol. 14 (2008), 72-80.
6. T.M. Wang, J.T. Xi, and Y.Jin, A Model Research for Prototype Warp Deformation in the FDM Process, *International Journal of Advanced Manufacturing Technology*, Vol. 33 (2007), 1087-1096.
7. A.M. Yardimci et al, Numerical Modeling of Fused Deposition Processing, *Proceedings of the ASME Materials Division*, Vol. 69 (1995), 1225-1235.
8. C. Bellehumeur, L. Li, Q. Sun, and P. Gu, Modeling of Bond Formation Between Filaments in the Fused Deposition Modeling Process, *Journal of Manufacturing Processes*, Vol. 6 (2004), 170-178.

9. O. Pokluda, C. Bellehumeur, and J. Vlachopoulus, Modification of Frenkel's Model for Sintering, *AIChE Journal*, Vol. 43 (1997), 3253-3256.
10. S.H. Ahn, C. Baek, S. Lee, and S. Ahn, Anisotropic Tensile Failure Model of Rapid Prototyping Parts-Fused Deposition Modeling (FDM), *International Journal of Model Physics B*, Vol. 17 (2002), 1510-1516.
11. J. Rodriguez, J. Thomas, and J. Renaud, Design of Fused-Deposition ABS Components for Stiffness and Strength, *Journal of Mechanical Design*, Vol. 125 (2003), 545-551.
12. Y. Zhang and K. Chou, A Parametric Study of Part Distortions in Fused Deposition Modelling Using Three-Dimensional Finite Element Analysis, *Proceedings of the Institution of Mechanical Engineers, Part B, Journal of Engineering Manufacture*, Vol. 222 (2008), 959-968.
13. Y. Zhang and K. Chou, Three-Dimensional Finite Element Analysis Simulations of the Fused Deposition Modelling Process, *Proceedings of the Institution of Mechanical Engineers, Part B, Journal of Mechanical Engineering Science*, Vol. 220 (2006), 1663-1671.
14. W. Zhong et al, Short Fiber Reinforced Composites for Fused Deposition Modeling, *Materials Science and Engineering*, Vol. 301 (2001), 125-130.
15. M.L. Shofner, K. Lozano, F.J. Rodriguez-Macias, and E.V. Barrera, Nanofiber-Reinforced Polymers Prepared by Fused Deposition Modeling, *Journal of Applied Polymer Science*, Vol. 89 (2003), 3081-3090.
16. Personal correspondence, Mike Hayes, The Boeing Company, St. Louis, MO, Sept 2009.
17. RADEL polyphenylsulfone, Solvay Advanced Polymers, 15 Mar. 2010, Web, 14 Apr. 2010.
18. Radel R (Polyphenylsulfone-PPSU), Plastics International, Web, 14 Apr. 2010.

19. Y.J. Bhandari, R.R. Gallucci, M. Sanner, and R. Singh, Polyetherimide-Polyestercarbonate Blends with Low Heat Release, *ANTEC 2008*, (2008), 1791-1795.
20. Y.J. Bhandari, R.R. Gallucci, M. Sanner, and R. Singh, Polyetherimide-Polyestercarbonate Blends with Low Heat Release, Sabic Innovative Plastics, *Microsoft PowerPoint* file, 8 Mar. 2010.
21. DatapointLabs Report # 11719-11724: R-11769 (6 Materials), DatapointLabs, 95 Brown Road, Ithaca, NY 14850, 7 Apr. 2007.
22. S.F. Costa, F.M. Duarte, and J.A. Covas, Towards Modelling of Free Form Extrusion: Analytical Solution of Transient Heat Transfer, *International Journal of Material Forming*, Vol. 1 (2008), 703-706.
23. 9085 Data, The Boeing Company, *Microsoft Excel* file, 27 Jan. 2010.
24. Personal correspondence, Mike Hayes, The Boeing Company, St. Louis, MO, Jan. 2010.
25. A. B. Blyumenfeld, E.V. Kalugina, and G.E. Zaikov, Structure Thermal Stability and Thermal Stabilization of the Engineering Polyimide and Polysulfone Resins, *International Journal of Polymeric Materials*, Vol. 44 (1999), 95-105.
26. Y.L. Zhao et al, Mechanisms of Thermal Decompositions of Polysulfones: A DFT and CBS-QB3 Study, *Macromolecules*, Vol. 38 (2005), 10279-10285.
27. Personal correspondence, Gregg Bogucki, the Boeing Compnay, St. Louis, MO, Nov. 2009.
28. S. Carroccio, C. Puglisi, and G. Montaudo, Mechanisms of Thermal Oxidation in Poly(bisphenol A carbonate), *Macromolecules*, Vol. 35 (2002), 4297-4305.
29. B.N. Jang and C.A. Wilkie, A TGA/FTIR and mass spectral study on the thermal degradation of bisphenol A polycarbonate, *Polymer Degradation and Stability*, Vol. 86 (2004) 419-430.

30. L. Perng, Thermal Decomposition Characteristics of Poly(ether imide) by TG/MS, *Journal of Polymer Research*, Vol. 7 (200), 185-193.
31. S. Carroccio, C. Puglisi, and G. Montaudo, New Vistas in Polymer Degradation. Thermal Oxidation Processes in Poly(ether imide), *Macromolecules*, Vol. 38 (2005), 6849-6862.
32. Air Properties, The Engineering Toolbox, Web, 14 Mar. 2009.
33. C.T. Bellehumeur, M. Kontopoulou, and J. Vlachopoulos, The Role of Viscoelasticity in Polymer Sintering, *Rheo Acta*, Vol. 37 (1998), 270-278.
34. A. Bellini, S. Guceri, and M. Bertoldi, Liquifier Dynamics in Fused Deposition, *Journal of Manufacturing Science and Engineering*, Vol. 126 (2004), 237-246.
35. S.H. Ahn et al, Anisotropic Tensile Failure Model of Rapid Prototyping Parts – Fused Deposition Modeling (FDM), *International Journal of Modern Physics B*, Vol. 17 (2003), 1510-1516.
36. Y. Jin, J. Zhang, Y. Wang, and Z. Zhu, Filament Geometrical Model and Nozzle Trajectory Analysis in the Fused Deposition Modeling Process, *Journal of Zheijiang University SCIENCE A*, Vol. 10 (2009), 370-376.
37. S. Mazur and D.J. Plazek, Viscoelastic Effects in the Coalescence of Polymer Particles, *Progress in Organic Coatings*, Vol. 24 (1994), 225-236.
38. L. Li, Q. Sun, C. Bellehumeur, and P. Gu, Composite Modeling and Analysis for Fabrication of FDM Prototypes with Locally Controlled Properties, *Journal of Manufacturing Processes*, Vol. 4 (2002), 129-139.

Appendices

Appendix A — Material Properties Data

Table A.1. Experimental data for temperature dependent thermal conductivity (PPSF) [21].

T (K)	k (W/m-K)
317.00	0.1780
338.00	0.1820
358.67	0.1917
379.00	0.2010
399.33	0.2037
419.33	0.2150
439.00	0.2183
459.00	0.2273
478.33	0.2553
497.67	0.2657
517.33	0.2777
537.33	0.2803
557.33	0.2817
577.00	0.2857
616.67	0.2880

Table A.2. Experimental data for temperature dependent specific heat capacity (PPSF) [21].

T (K)	Cp (J/kg-K)
303.00	1069.3
394.67	1217.0
485.67	1490.3
491.33	1560.7
492.67	1588.0
608.00	1890.3
721.00	2101.3

Table A.3. Experimental data for temperature dependent kinematic viscosity (PPSF) [21].

T (K)	nu (Pa-s)
553.00	439.636
573.00	220.868
593.00	121.530
623.00	49.947

Table A.4. Experimental data for temperature dependent thermal conductivity (Ultem) [22].

T (K)	k (W/m-K)
310	0.186
317	0.176
338	0.182
358	0.184
378	0.199
399	0.201
418	0.196
438	0.228
458	0.222
477	0.194
498	0.226
518	0.242
537	0.228
557	0.244

Table A.5. Experimental data for temperature dependent specific heat capacity (Ultem) [22].

T (K)	Cp (J/kg-K)
294	34.5
322	1200.0
354	1272.5
386	1365.2
418	1477.2
450	1656.4
482	1931.3
514	2027.1
546	2104.4
578	2174.1
610	2253.4
642	2351.7
674	2451.1

Table A.6. Experimental data for temperature dependent kinematic viscosity (Ultem) [22].

T (K)	nu (Pa-s)
593	1194.0
663	1360.5
673	1400.0
683	1438.3
693	2215.6

Appendix B — Air Properties

Table B.1. Temperature dependent values of thermal conductivity, kinematic viscosity, expansion coefficient, and Prandtl number [32].

T (K)	k (W/m-K)	nu (Pa-s)*10^(-6)	beta (1/K)	Pr
473	0.039	34.63	2.11	0.685
523	0.042	41.14	1.91	0.680
573	0.045	47.85	1.75	0.680

Appendix C — Matlab M-files

C.1. M-file: d1_cooling.m

```
%User Defined function that calculates rate of cooling for a single
%filament in one dimension.  All input and output temperatures are in
%Kelvin.

function [T t]=d1_cooling(To,Tinf,dt,tfinal,flag)

%flag dicates material used, "1" is PPSF, "2" is Ultem 9085
    if flag==1
        matl='PPSF';
        %Create fits for PPSU and air properties, where kspline is
thermal
        %conductivity of PPSU and Cppoly is the polyfit of Cp for PPSU

        %Specific Heat Capacity [J/kgK]of PPSU B1
        B1_Cp_T1=[30 124 217 223 225 337 448];
        B1_Cp_T1=B1_Cp_T1+273;
        B1_Cp1=[1116 1246 1568 1600 1643 1903 2198];
        Cp1poly=polyfit(B1_Cp_T1,B1_Cp1,1);

        B1_Cp_T2=[30 121 211 217 218 334 448];
        B1_Cp_T2=B1_Cp_T2+273;
        B1_Cp2=[1005 1169 1422 1523 1544 1859 1992];
```

```
Cp2poly=polyfit(B1_Cp_T2,B1_Cp2,1);

B1_Cp_T3=[30 120 210 215 216 334 448];
B1_Cp_T3=B1_Cp_T3+273;
B1_Cp3=[1087 1236 1481 1559 1577 1909 2114];
Cp3poly=polyfit(B1_Cp_T3,B1_Cp3,1);

%Average polynomial
Cppoly=[mean([Cp1poly(1) Cp2poly(1) Cp3poly(1)])...
mean([Cp1poly(2) Cp2poly(2) Cp3poly(2)])];

%Thermal conductivity [W/mK] of PPSU B1
B1_k_T1=[44 65 85 106 126 146 166 186 205 224 244 264 284 304
343];
B1_k_T1=B1_k_T1+273;
B1_k1=[.169 .177 .182 .201 .201 .209 .216 .225 .267 .267 .274
.281 .278 .286 .287];

B1_k_T2=[44 65 86 106 126 146 166 186 206 225 244 264 284 304
343];
B1_k_T2=B1_k_T2+273;
B1_k2=[.185 .181 .195 .203 .208 .222 .222 .228 .249 .271 .281
.276 .284 .285 .293];

B1_k_T3=[44 65 86 106 127 147 166 186 205 225 245 265 285 304
345];
B1_k_T3=B1_k_T3+273;
```

```
    B1_k3=[.180 .188 .198 .199 .202 .214 .217 .229 .250 .259 .278
    .284 .283 .286 .284];

    %Average polynomial
        for i=1:length(B1_k1)
            kTavg(i)=mean([B1_k_T1(i) B1_k_T2(i) B1_k_T3(i)]);
            kavg(i)=mean([B1_k1(i) B1_k2(i) B1_k3(i)]);
        end

    kspline=spline(kTavg,kavg);
elseif flag==2
    matl='Ultem 9085';
    Cp_T=21:4:417;
    Cp_T=Cp_T+273;
    Cp =1.0e+003 * [0.0345 0.8409 1.1010 1.1462 1.1616 1.1764
    1.1880 1.2000 1.2107 1.2188 1.2253 1.2328 1.2411 1.2518
    1.2612 1.2725 1.2833 1.2927 1.3037 1.3147 1.3255 1.3358 1.3500
    1.3652 1.3779 1.3913 1.4051 1.4182 1.4316 1.4464 1.4615...
    1.4772 1.4933 1.5079 1.5239 1.5365 1.5541 1.5770 1.6079...
    1.6564 1.7262 1.8190 1.8896 1.9207 1.9139 1.9151 1.9221...
    1.9313 1.9418 1.9509 1.9626 1.9743 1.9887 2.0027 2.0165...
    2.0271 2.0273 2.0369 2.0469 2.0583 2.0668 2.0805 2.0872...
    2.1044 2.1166 2.1266 2.1367 2.1436 2.1501 2.1606 2.1691...
    2.1741 2.1810 2.1900 2.1991 2.2126 2.2238 2.2323 2.2408...
    2.2534 2.2669 2.2777 2.2864 2.2991 2.3120 2.3237 2.3476...
    2.3517 2.3619 2.3784 2.3868 2.4003 2.4211 2.4356 2.4451...
    2.4511 2.4550 2.4546 2.4582 2.4526];
```

```
        Cp_spline=spline(Cp_T,Cp);

        k_T=[37 44 65 85 105 126 145 165 185 204 225 245 264 284];
        k_T=k_T+273;
        k_vals=[0.1860 0.1760 0.1820 0.1840 0.1990 0.2010 0.1960 0.2280
        0.2220 0.1940 0.2260 0.2420 0.2280 0.2440];

        k_poly=polyfit(k_T,k_vals,1);

    end
%Air properties
T_air_props=273+[200 250 300];
k_air=[0.039 0.042 0.045];
nu_air=[34.63 41.14 47.85]*10^(-6);
beta_air=[2.11 1.91 1.75];
Pr_air=[0.685 0.68 0.68];

k_a_pol=polyfit(T_air_props,k_air,1);
nu_a_pol=polyfit(T_air_props,nu_air,1);
beta_a_pol=polyfit(T_air_props,beta_air,2);
Pr_a_pol=polyfit(T_air_props,Pr_air,1);

%Initialize relevant variables for iterative loop
T(1)=To;
Tnew=To;
Nuo=0.36;
```

```
%Geometry props
a=.02*.0254;
b=.01*.0254;
lambda=(a-b)/(a+b);
P=pi*(a+b)*((64-3*lambda^4)/(64-16*lambda^2));
A=pi*a*b;
i=1;
%Start iterative loop calculating time with temperature, iterating on
%temperature dependent properties of PPSU and air.
for t=0:dt:tfinal
    error=1;

    while error > 1e-6
        Told=Tnew;
        if flag==1
            k=ppval(kspline,Told);
            Cp=polyval(Cppoly,Told);
            rho=1300;
        elseif flag==2
            k=polyval(k_poly,Told);
            Cp=ppval(Cp_spline,Told);
            rho=1340;
        end

        k_a=polyval(k_a_pol,Told);
        nu_a=polyval(nu_a_pol,Told);
        beta_a=polyval(beta_a_pol,Told);
        Pr_a=polyval(Pr_a_pol,Told);
```

```
        Gr=9.8*beta_a*(Told-Tinf)*(4*A/P)^3/(nu_a)^2;

Nu=(sqrt(Nuo)+((Gr*Pr_a/300)/(1+(0.5/Pr_a)^(9/16))^(16/9))^(1/6))^2;
        hconv=k_a*Nu/(4*A/P);
        hcond=0;
        h=hconv+hcond;
        alpha=k/(rho*Cp);
        beta=h*P/(rho*Cp*A);
        m=(sqrt(1+4*alpha*beta)-1)/(2*alpha);
        Tnew=Tinf+(To-Tinf)*exp(-m*t);
        error=abs(Tnew-Told)/Told;
    end
    T(i)=Tnew;
    i=i+1;
end


t=0:dt:tfinal;
figure
plot(t,T);
%title(['Single Filament Cooling: To=' num2str(To) ', Tinf='
num2str(Tinf) ' (' matl ')']);
xlabel('Time (s)');
ylabel('Temperature (degrees K)');


end
```

C.2. M-file: d1_bonding.m

```
%This m-file is a predictive model for the bonding of PPSF during the
FDM
%process.  All input and output temperatures are in Kelvin.

function [bond_final,bond,t_bond]=d1_bonding(To,Tinf,dt,tfinal,flag)

[T t]=d1_cooling(To,Tinf,dt,tfinal,flag);

if flag==1
    matl='PPSF';
%PPSF viscosity
    %Surface Tension (N/m)
    gamma=.0475;

    %Viscosity (Pa-s)
    %Find average polynomials at various temps and shear rates
    shear_rate=[100 200 500 1000 2000 5000 10000];
    eta_280_1=[445.80 433.59 395.73 336.45 252.51 145.09 88.48];
    eta_300_1=[225.96 229.01 223.51 199.67 166.71 110.04 71.57];
    eta_320_1=[128.25 125.19 120.92 116.02 106.56 50.07 57.16];
    eta_350_1=[54.96 61.07 59.85 58.62 55.87 47.26 36.33];

    eta_280_2=[421.38 418.32 384.73 326.68 249.15 143.75 88.30];
    eta_300_2=[219.85 222.90 216.18 198.45 163.35 109.06 71.32];
    eta_320_2=[116.03 125.19 125.80 120.29 107.17 78.16 56.00];
```

```
    eta_350_2=[48.86 54.96 59.85 58.01 54.96 46.16 35.17];

    for i=1:length(shear_rate)
        eta_280(i)=mean([eta_280_1(i),eta_280_2(i)]);
        eta_300(i)=mean([eta_300_1(i),eta_300_2(i)]);
        eta_320(i)=mean([eta_320_1(i),eta_320_2(i)]);
        eta_350(i)=mean([eta_350_1(i),eta_350_2(i)]);
    end

    %Find eta at 0 shear rate for each temperature
    eta_fit(1)=interp1(shear_rate,eta_280,0,'cubic','extrap');
    eta_fit(2)=interp1(shear_rate,eta_300,0,'cubic','extrap');
    eta_fit(3)=interp1(shear_rate,eta_320,0,'cubic','extrap');
    eta_fit(4)=interp1(shear_rate,eta_350,0,'cubic','extrap');

    %Create temp points for interpolation
    eta_temp=[280 300 320 350];
    eta_temp=eta_temp+273;

elseif flag==2
    matl='Ultem 9085';
    %Ultem viscosity calculations
    %Surface Tension (N/m)
    gamma=.0342;

    %Viscosity (Pa-s)
    %Find average polynomials at various temps and shear rates
    shear_rate=[10.02 20.04 50 99.99 200 500 1000 2000 5000 10000];
```

```
    eta_320=[1158 761.6 732.8 659.5 558.8 399.4 310.8 202.1 132.8
    86.59];
    eta_390=[1066 533.1 213.7 125.2 83.97 61.68 63.2 51.91 34.99
    23.57];
    eta_400=[1097 548.4 219.8 119.1 71.76 44.58 46.1 40.61 26.81
    20.09];
    eta_410=[1127 563.6 226 119.1 70.23 36.64 24.12 17.59 14.84 13.46];
    eta_420=[1736 868.2 348.1 167.9 83.97 37.25 23.51 18.78 12.95
    9.954];

    %Find eta at 0 shear rate for each temperature
    eta_fit(1)=interp1(shear_rate,eta_320,0,'cubic','extrap');
    eta_fit(2)=interp1(shear_rate,eta_390,0,'cubic','extrap');
    eta_fit(3)=interp1(shear_rate,eta_400,0,'cubic','extrap');
    eta_fit(4)=interp1(shear_rate,eta_410,0,'cubic','extrap');
    eta_fit(5)=interp1(shear_rate,eta_420,0,'cubic','extrap');

    %Create temp points for interpolation
    eta_temp=[320 390 400 410 420];
    eta_temp=eta_temp+273;

end
    %Loop using Runge-Kutta (RK4)

    %Initial values
    theta(1)=0;
    if flag==1
        %Exponential fit achieved with Microsoft Excel
```

```
    eta=1e10*exp(-0.031*T(3));
elseif flag==2
    eta=interp1(eta_temp,eta_fit,T(3),'cubic','extrap');
end

%Calculate equivalent radius (ao) of the elliptical filament
maj_ax=.02*.0254;
min_ax=.01*.0254;
ecc=sqrt(1-(min_ax/maj_ax)^2);
perim=maj_ax/2*sqrt(93+0.5*sqrt(3));
area=pi*maj_ax*min_ax;
ao=2*area/perim;
theta(2)=sqrt((dt/10)*gamma/(eta*ao));

for i=4:2:(tfinal/dt-1)
    if flag==1
        eta_1=1e10*exp(-0.031*T(i-1));
    elseif flag==2
        eta_1=interp1(eta_temp,eta_fit,T(i-1),'cubic','extrap');
    end
    theta_1=theta(i/2);
    k1=(gamma/(ao*eta_1))*(2^(-5/3)*cos(theta_1)*sin(theta_1)*...
        (2-cos(theta_1)^(1/3)))/((1-cos(theta_1))*...
        (1+cos(theta_1))^(1/3));
    if flag==1
        eta_2=1e10*exp(-0.031*T(i));
    elseif flag==2
        eta_2=interp1(eta_temp,eta_fit,T(i),'cubic','extrap');
```

```
    end
    theta_2=theta(i/2)+(1/2)*dt*k1;
    k2=(gamma/(ao*eta_2))*(2^(-5/3)*cos(theta_2)*sin(theta_2)*...
        (2-cos(theta_2)^(1/3)))/((1-cos(theta_2))*...
        (1+cos(theta_2))^(1/3));
    if flag==1
        eta_3=1e10*exp(-0.031*T(i));
    elseif flag==2
        eta_3=interp1(eta_temp,eta_fit,T(i),'cubic','extrap');
    end
    theta_3=theta(i/2)+(1/2)*dt*k2;
    k3=(gamma/(ao*eta_3))*(2^(-5/3)*cos(theta_3)*sin(theta_3)*...
        (2-cos(theta_3)^(1/3)))/((1-cos(theta_3))*...
        (1+cos(theta_3))^(1/3));
    if flag==1
        eta_4=1e10*exp(-0.031*T(i+1));
    elseif flag==2
        eta_4=interp1(eta_temp,eta_fit,T(i+1),'cubic','extrap');
    end
    theta_4=theta(i/2)+dt*k3;
    k4=(gamma/(ao*eta_4))*(2^(-5/3)*cos(theta_4)*sin(theta_4)*...
        (2-cos(theta_4)^(1/3)))/((1-cos(theta_4))*...
        (1+cos(theta_4))^(1/3));
    theta(i/2+1)=theta(i/2)+(1/6)*dt*(k1+2*k2+2*k3+k4);
end


bond=ao*sin(theta);
t_bond=0:dt*2:(tfinal-dt*2);
```

```
    figure
    plot(t_bond,bond);
    %title(['Adjacent Filament Bonding: To=' num2str(To) ', Tinf='
num2str(Tinf)]);
    xlabel('Time (s)');
    ylabel('Bond Length (m)');
    bond_final=bond(end);
end
```